Published in final edited form as:

Curr Biol. 2020 January 20; 30(2): 264–275.e8. doi:10.1016/j.cub.2019.11.075.

Circuit mechanisms underlying chromatic encoding in *Drosophila* photoreceptors

Sarah L. Heath[a,1], **Matthias P. Christenson**[a,1], **Elie Oriol**[b], **Maia Saavedra-Weisenhaus**[a], **Jessica R. Kohn**[a], **Rudy Behnia**[a,*]

[a]Zuckerman Institute for Mind Brain Behavior, Department of Neuroscience, Columbia University, 3227 Broadway, New York, NY, 10027, United States

[b]Département de Physique, Ecole Normale Supérieure, 24 Rue Lhomond, Paris, 75005, France

Summary

Spectral information is commonly processed in the brain through generation of antagonistic responses to different wavelengths. In many species, these color opponent signals arise as early as photoreceptor terminals. Here, we measure the spectral tuning of photoreceptors in *Drosophila.* In addition to a previously described pathway comparing wavelengths at each point in space, we find a horizontal-cell-mediated pathway similar to that found in mammals. This pathway enables additional spectral comparisons through lateral inhibition, expanding the range of chromatic encoding in the fly. Together, these two pathways enable efficient decorrelation and dimensionality reduction of photoreceptor signals, while retaining maximal chromatic information. A biologically constrained model accounts for our findings and predicts a spatio-chromatic receptive field for fly photoreceptor outputs, with a color opponent center and broadband surround. This dual mechanism combines motifs of both an insect-specific visual circuit and an evolutionarily convergent circuit architecture, endowing flies with the unique ability to extract chromatic information at distinct spatial resolutions.

In Brief

Heath *et al.* show that color opponency in fly photoreceptors is the result of an evolutionary convergent horizontal-cell-mediated pathway and an insect-specific pathway. These allow the visual system to build an efficient yet comprehensive representation of chromatic information, and are predicted to give rise to a complex spatial receptive field.

* Lead Contact: rb3161@columbia.edu.

[1]Contributed equally

Author Contributions

RB, SLH, and MPC conceived of experiments and wrote the manuscript. SLH acquired the imaging data. SLH and MSW acquired optogenetic data and performed animal husbandry. MPC processed and analyzed the imaging data, wrote the visual stimulation code, and performed the modeling work. EO built the flyback system. MSW and EO acquired immunohistochemistry data. MSW and JRK genotyped flies.

Declaration of Interests

The authors do not declare any conflicts of interest.

Graphical Abstract

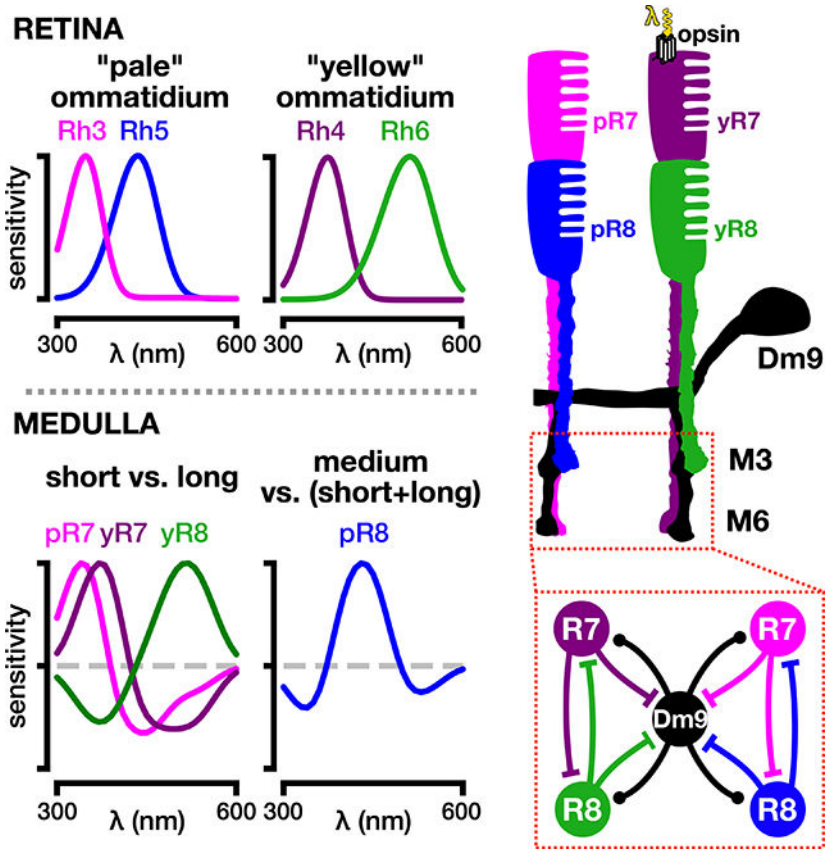

Keywords

color vision; *Drosophila melanogaster*; photoreceptor; medulla; neural circuit; color opponency; photon capture

Introduction

Color vision is an important source of visual information, enhancing our recognition of objects in complex visual fields. How is wavelength information extracted by the brain? A single type of photoreceptor cannot distinguish wavelength independently of the intensity of light because different spectral distributions of varying intensity can give rise to the same photoreceptor output [1]. Generally, color percepts can only be extracted by comparing the output from at least two photoreceptors with different spectral sensitivities. This comparison is apparent in color opponent neurons, which receive antagonistic inputs from different photoreceptor types and therefore exhibit opposing responses to different ranges of wavelengths [2]. Our understanding of the neural processes that lead to our perception of colors therefore critically depends on our understanding of color opponent signals and the underlying circuits that establish them. Moreover, opponent processing motifs extend to other sensory systems, such as olfaction [3], which further highlights the importance of

unraveling this type of antagonistic signaling in the more general context of sensory processing.

Much of what we know about the properties of color opponent neurons comes from work done in the tri-chromatic retina of primates. There, the signals from L, M and S cones, named for their sensitivity in the long, middle and short wavelength regions of the spectrum, are combined by two main types of opponent retinal ganglion cells (RGCs): the so-called “red-green” neurons, which compare the activity of M and L photoreceptors, and “blue-yellow” neurons, which compare the activity of S and L+M photoreceptors (reviewed in [4]). Because cone photoreceptors are arranged in a 2D lattice, lateral interactions are essential for establishing these opponent signals in the retina. This results in spectrally opponent signals in RGCs which compare chromatic information between neighboring points in visual space through center-surround interactions. Interestingly, the two axes of opponency - “red-green” and “blue-yellow” - encoded at the level of RGCs have been shown to correspond to an optimal decomposition of S, M and L cone sensitivities [5]. This allows the retina to remove the correlations introduced by the high degree of overlap between cone sensitivities and more efficiently transmit spectral information to downstream visual circuits.

Opponent signals have been measured across the animal kingdom, reinforcing the importance of this operation in color circuits across evolution. *Drosophila melanogaster* has emerged as a genetically tractable system to study circuit level mechanisms of color vision [6, 7, 8, 9, 10, 11], and color opponent signals have been measured at the axonal terminals of cone-like photoreceptors in the fly brain [6]. However, unlike the 2D lattice photoreceptor arrangement found in mammals, the light sensing rhabdomeres of fly cone-like photoreceptors R7 and R8 are positioned one on top of another [12] (Figure 1A). This architecture allows photoreceptors in each optical unit, or ommatidium, to absorb photons emanating from the same point in visual space. A specialized circuit taking advantage of this configuration was recently described to generate color opponent signals through reciprocal inhibition between pairs of R7 and R8 photoreceptors from a single ommatidium [6], allowing for pixel-by-pixel comparison of wavelengths. Because of the spectral composition of the fly eye, these intra-ommatidial interactions impose specific constraints on the types of spectral comparisons that the circuit can make. There are two types of ommatidia in the main part of the fruit fly eye, that are distributed in a stochastic pattern (65% “yellow”, 35% “pale”, Figure 1A, D) (reviewed in [13]). “Pale” ommatidia express the short-UV-sensitive Rh3 rhodopsin in R7 and the blue-sensitive Rh5 in R8. “Yellow” ommatidia express the long-UV-sensitive Rh4 rhodopsin in R7 and the green-sensitive Rh6 in R8. An opponent mechanism purely based on intra-ommatidial interactions therefore defines two separate color opponent channels, both comparing spectral information along a UV versus visible axis.

This architecture has the advantage of allowing chromatic information to be extracted at the full resolution of the eye, similarly to achromatic pathways driven by R1–6 photoreceptors [14], which express the broadband opsin Rh1 (Figure 1A, D). However, it does not allow for additional comparisons to be made in the spectral domain, such as those between the blue and green part of the spectrum, which appear to be used behaviorally [7, 9, 11], and which may be beneficial in terms of efficient signal processing. Lateral interactions between R7s

and R8s from neighboring ommatidia, akin to those mediated by horizontal cells in the mammalian retina [15], would allow for increased resolution of chromatic pathways in the spectral domain and provide the fly with more flexible mechanisms for encoding chromatic information.

Here, we measure the spectral tuning of all four types of wavelength-specific photoreceptors in the fly visual system. We find that each R7 and R8 photoreceptor type displays specific and distinct wavelength opponent properties, which cannot be explained solely by previously described reciprocal inhibition within single ommatidia. At the circuit level, we show that indirect antagonistic interactions between R7s and R8s from neighboring ommatidia also contribute to shaping the spectral tuning of all photoreceptor outputs, and that these interactions are mediated by the horizontal-cell-like medulla interneuron Dm9. Indirect interactions enable additional comparisons in the spectral domain which correspond to efficient decorrelation and dimensionality reduction of the spectral sensitivities of *Drosophila* opsins. In addition, we build a linear recurrent model constrained by the underlying circuit interactions. This model accurately predicts our observed responses, while also showing that electron-microscopy-based synaptic count provides an accurate proxy for synaptic weight in this early processing step in color circuits. Finally, our circuit model predicts a receptive field for R7 and R8 outputs with a broadband surround superimposed on a color-opponent center, combining the motifs of both an evolutionarily convergent circuit architecture and an insect-specific visual circuit.

Results

R7 and R8 inputs are transformed into opponent outputs through interactions between photoreceptor types

Color opponent responses are established via antagonistic interactions of inputs from different types of photoreceptors. In the case of *Drosophila* photoreceptors R7 and R8, rhabdomeric responses of these photoreceptors in the eye can be considered inputs, and their color opponent axonal responses in the medulla can be considered outputs (Figure 2A). To understand how inputs are combined to give rise to color opponent outputs, our first goal was to measure and compare the rhabdomeric and the axonal spectral tuning properties of these photoreceptors.

In vivo two-photon imaging of genetically targeted GCaMP6f in R7 and R8 photoreceptors allows for straightforward measurement of their axonal outputs in the M6 and M3 layers of the medulla, respectively (Figure 1B). However, we could not visualize rhabdomeres in the eye with our imaging setup, and could therefore not directly measure rhabdomeric responses. Instead, we used genetic tools to make indirect measurements of putative rhabdomeric responses. Because these responses are transformed into axonal outputs through interactions with other photoreceptor types [6], we reasoned that measurements at the axonal level in mutant flies where these interactions are abolished, which correspond to cell autonomous responses, can be considered equivalent to putative rhabdomeric responses. For this set of experiments, we isolated these responses in mutant flies where only the imaged photoreceptor type is active, effectively preventing external inhibitory input from other photoreceptor types. This is done by functionally rescuing phototransduction in single

photoreceptor types in the blind *norpa-* mutant background by driving expression of UAS-NorpA with Rhodopsin-Gal4 drivers [16].

In order to compare putative rhabdomeric and axonal tuning, we developed a method to measure spectral tuning curves (Figure 1D–G). Specifically, we measured neuronal responses to a range of relatively narrow-band light sources of equal photon flux (E = moles of photons per m^2 per s) spanning the fly's visible spectrum. Instead of using a system with a large number of different light sources, we devised a method that allows us to measure tuning curves using only a limited number of LEDs. For a given light source, each photoreceptor type will "capture" a specific number of photons. This number, or photon capture, is calculated as a function of each opsins sensitivity and the spectrum of the light source ([17, 18]; see STAR methods; Equation 5). We simulated the effect of this particular light source on the fly eye by showing a combination of the six LEDs in our stimulus setup, which evoked the same capture in each of the five photoreceptor types as the intended narrow-band light source (see STAR methods and Figure S1 for details on implementation and accuracy). All experiments were performed in light adapted conditions where the simulated light source is presented over a background light. Measuring responses to these simulated light sources across the spectrum allowed us to construct spectral tuning curves for a given cell type.

As expected from the spectral sensitivity of the opsins they express, the putative rhabdomeric responses we measured show UV sensitivity in p/yR7 peaking at 360 nm and 380 nm, respectively, blue sensitivity in pR8 peaking at 420 nm, and blue/green sensitivity in yR8 peaking at 500 nm (Figure 2B–E). These neural responses are directly related to spectral sensitivities of the opsins that these photoreceptors express. It was previously shown that a logarithmic transformation of photon capture corresponds to the transformation of light absorption of a photoreceptor by the phototransduction cascade [19, 20]. We thus compared the tuning curves we obtained to the log of the relative photon capture log (q) in each rhodopsin, specifically calculated for the presented stimuli. We found that the measured tuning curves closely match the calculated log (q). This result shows that log (q) is a reliable estimate of the putative rhabdomeric responses we measured in this system, and we will subsequently refer to log (q) as the calculated rhabdomeric response.

In the case of axonal responses in wild type flies, we measured spectrally opponent waveforms in all photoreceptor types (Figure 2F–I). pR7s outputs are activated by UV spanning 320–420 nm, and inhibited by longer wavelengths (Figure 2F, J). yR7 outputs are also activated by UV, with their response remaining excitatory up to 440 nm, and becoming inhibitory from 480 nm onwards (Figure 2G, K). pR8 outputs are the only ones to show a tri-lobed spectral tuning (Figure 2H, L). They are activated by blue light ranging from 400–500 nm and inhibited in the UV from 320–380 nm, as well as in the green from 530–620 nm. yR8 outputs are activated by wavelengths covering the wide range of 400–620 nm in the blue/green but inhibited by UV from 320–380 nm (Figure 2I, M).

Each R7 and R8 terminal type thus displays distinct and specific wavelength opponent properties that are dependent on interactions between photoreceptors with different spectral sensitivities. This is generally consistent with previous work. Schnaitmann et al. [6] found

that opponent signals at the level of R7 and R8 outputs are generated through both direct and indirect antagonistic interactions between pairs of R7 and R8 photoreceptors from a single ommatidium: direct interactions in the form of reciprocal histaminergic inhibition, and indirect, inhibitory interaction mediated by a yet-to-be-identified medulla interneuron. However, we measured opponency in ranges that are not predicted by reciprocal inhibition exclusively between R7 and R8 photoreceptors from the same ommatidium. This is most obvious in the case of pR7 and pR8. Indeed, both of these photoreceptor types are inhibited by green light (> 540 nm) (Figure 2F, H), whereas our measurements of their putative rhabdomeric responses show that neither responds at these long wavelengths (Figure 2B, D). Intra-ommatidial interactions (between R7 and R8 from the same ommatidium) alone are therefore not sufficient to explain the spectral tuning properties we measure. We next aimed to further define the circuit mechanisms that combine and process R7 and R8 signals to give rise to the diverse spectrally opponent axonal responses that we measured.

Both intra- and inter-ommatidial antagonistic interactions shape the spectral tuning properties of R7 and R8 outputs

According to our putative rhabdomeric measurements (Figure 2B–E), the inhibition measured in pR7 and pR8s axons in the long wavelength range can only originate from yR8, or the broadband photoreceptors R1–6. Thus, we hypothesized that inter-ommatidial interactions (between R7s and R8s from neighboring ommatidia) and/or inputs from R1–6 contribute to the spectral tuning of R7 and R8 outputs. We employed genetic methods to determine the contribution of specific photoreceptor types to the spectral tuning of R7 and R8 outputs. We took advantage of *norpa-* mutants and selectively rescued NorpA in pairwise combinations of photoreceptor types.

First, we imaged pR7 in flies in which pR7 function was restored in combination with one other photoreceptor subtype. The tuning curve of pR7 in flies when phototransduction is rescued in both pR7 and pR8 is similar to that of wild type pR7 in that there is activation in the UV range (320–400 nm) and inhibition in the blue range (420–460 nm) (Figure 3A).This is consistent with intra-ommatidial inhibition from pR8, as the putative rhabdomeric responses of pR8 show blue sensitivity (Figure 2D). However, inhibition is lost in the long wavelengths (> 540 nm). In contrast, in a pR7/yR8 rescue, the tuning curve for pR7 displays clear inhibitory responses at all wavelengths above 420 nm (Figure 3C), showing that yR8 contributes to blue/green inhibition in pR7 through inter-ommatidial interactions. In a pR7/yR7 rescue, pR7s are inhibited in the UV/blue range (400–450 nm) (Figure 3B), showing that yR7s contribute to pR7 responses. These results demonstrate that, in addition to intra-ommatidial interactions from pR8, inter-ommatidial interaction from both yR8 and yR7s contribute to opponent responses measured in pR7.

We performed the same set of experiments while imaging pR8 terminals. In a pR8/pR7 rescue, the tuning curve of pR8 becomes bi-lobed, showing inhibition only in the UV range (< 360 nm) and not in the green wavelength range (> 540 nm) (Figure 3D). Conversely, in a pR8/yR8 rescue, pR8 still shows inhibition to green but not to UV (Figure 3F). In a pR8/yR7 rescue, we did not see strictly inhibitory responses under our recording conditions, but we did observe a statistically significant decreased response in pR8 in the UV range (300–340

nm) in comparison to the calculated rhabomeric response (Figure 3E). This indicates that yR7 has an inhibitory effect on pR8. These results show that, similarly to pR7s, both intra-ommatidial and inter-ommatidial interactions contribute to the opponent responses measured in pR8s.

We next measured responses in all rescue combinations for yR7 and yR8. In experiments where yR7 was imaged, we confirmed antagonistic inputs from its intra-ommatidial partner yR8 in the green range (> 540 nm) but could not detect significant inhibition from pR8 or pR7 (Figure S2A–D). yR8 imaging confirmed antagonistic inputs from both p and y R7s in the UV range (< 380 and < 400, respectively), but no significant inhibition from pR8 was detected (Figure S2E–H).

Lastly, we investigated the possible contribution of R1–6 to the wild type signals by rescuing NorpA in each photoreceptor type separately together with R1–6. We found no significant differences in paired rescues with R1–6 compared to the measured putative rhabdomeric responses (Figure S2I–P), and thus did not consider R1–6 contributions further in our analysis.

Together, these experiments demonstrate that inhibitory interactions between R7 and R8 are not confined within medulla columns. Rather, there is a larger set of interactions between columns in the medulla that shape the tuning of R7 and R8 outputs, adding both additional spectral comparisons and a spatial dimension to opponent pathways.

The horizontal-cell-like Dm9 neuron mediates lateral, indirect opponency

The fact that opponent responses in R7s and R8s are shaped by inhibitory interactions between pale and yellow ommatidia is reminiscent of the circuit architecture of vertebrates, where horizontal cells mediate center-surround inhibitory interactions [15]. We thus hypothesized that inter-ommatidial inhibition in the fly medulla is similarly mediated by a horizontal cell-like interneuron in the circuit. The medulla interneuron in question should fulfill the following requirements: 1. be both pre- and post-synaptic to p/yR7s and p/yR8s, 2. span multiple columns (≥ 2) in the medulla, and 3. be excitatory, to enable opponent interactions through relief of excitation. Only one such neuron has been put forward by electron microscopy (EM) and RNAseq studies: Dm9 (Figure 4A) [21, 22, 23].

Dm9 is a multi-columnar medulla interneuron, spanning an average of seven columns and occupying distal medulla layers M1-M6 (Figure 4B, C, S3A–B). These cells tile in layers M2-M5 but overlap in M1 and M6 [24]. EM reconstructions show a large number of synapses from R7 and R8 onto to Dm9, as well as synapses from Dm9 back to both R7 and R8. In addition, Dm9s receive indirect inputs from R1–6 through the lamina monopolar cell L3, as well as inputs from the amacrine cell Dm8 [21]. Dm9 has been proposed to be an excitatory glutamatergic neuron [22].

To test whether Dm9 is functionally connected to photoreceptors, we optogenetically activated Dm9 using CsChrimson [25] while simultaneously imaging the activity of UV-sensitive R7s. The experiments were done in *norpa* blind flies to avoid the effects of activating the wild type opsins themselves. During CsChrimson activation using a red LED

(660nm), we observed depolarization of R7 photoreceptors in the experimental flies and not in the control flies (Figure 4D), thereby confirming a functional excitatory connection between Dm9 and photoreceptors.

Next, we measured the spectral tuning of Dm9. We found that Dm9 is inhibited by a broad range of wavelengths spanning the whole spectrum (Figure 4E–H). This is consistent with EM data showing that Dm9 gets inputs from all photoreceptor types. In addition to inhibition to light ON, Dm9 responds positively at light OFF, especially at high intensities of the stimulus. The origin of this OFF response is unclear, but could be due to L3 [26].

We then silenced the activity of Dm9 by expressing the inward-rectifying potassium channel Kir2.1 in these neurons specifically, while imaging from pR8 axons. We chose this particular photoreceptor type because it provides the clearest read-out of the effect of intra- or inter-ommatidial interactions. UV inhibition in pR8 is likely a combination of intra- and inter-ommatidial interactions, while long wavelength inhibition is due to inter-ommatidial interactions only. We therefore expected only a partial loss in UV opponency after Dm9 silencing, since direct intra-ommatidial inputs from pR7 should not be affected. Conversely, we expected complete loss of inhibition at the long wavelengths with complete Dm9 silencing, as we have shown that the source of these signals is purely inter-ommatidal. We found that when Dm9 activity is inhibited, inhibition in pR8 is overall reduced compared to the spectral tuning in wild type flies, and pR8 tuning is no longer tri-lobed (Figure 4I; S3C). These terminals still show opponency in the UV range (300–340 nm) compared to the calculated rhabdomeric response. However, opponency is lost in the green wavelength range (> 500 nm). This result is consistent with Dm9 mediating inter-ommatidial interactions.

In addition to these silencing experiments, we tested the role of Dm9 in this circuit by disrupting feedforward inhibition from photoreceptor to Dm9 specifically. Schnaitmann et al. [6] showed that direct axo-axonal inhibition is mediated by the histamine receptor HisCl1. As medulla neurons express the Ort histamine receptor and not HisCl1 [22], histaminergic transmission to medulla neurons (including Dm9) must be mediated by Ort. As expected, in a *ort-, hiscl1-* double mutant background we could not detect any inhibition in pR8 photoreceptors (Figure 4J, S3D). We then rescued ort expression exclusively in Dm9 neurons in this mutant background (Figure 4J). When imaging pR8 in these conditions, we found restored opponent waveforms both in the UV range (300–340 nm) and the green range (> 500 nm), showing that Dm9 is sufficient for mediating inter-ommatidial antagonism.

Our data combined with known connectivity indicates that the horizontal cell Dm9 mediates indirect intra- and inter-ommatidial inhibitory interactions.

Opponent mechanisms produce an efficient representation of chromatic information at the level of R7 and R8 outputs

Our data shows that inter-ommatidial antagonism, in addition to previously described intra-ommatidial antagonism, shapes the responses of the outputs of R7 and R8 photoreceptors. What are the consequences of this dual circuit on spectral encoding?

A clear consequence of opponency is a narrowing of the tuning of the responses in the medulla compared with their calculated rhabdomeric responses. To quantify this, we calculated correlation coefficients between the calculated rhabdomeric responses of R7 and R8 photoreceptors (Figure 5A) and between their measured axonal responses (Figure 5B). As expected from the high degree of overlap between the spectral sensitivities of the four opsins expressed in R7 and R8 (Figure 1D), there is a high degree of correlation between the calculated rhabdomeric responses. This effect is particularly pronounced for spectrally consecutive opsins such as Rh3 and Rh4 (0.97), Rh4 and Rh5 (0.82), and Rh5 and Rh6 (0.79). However, after antagonistic interactions have occurred in the medulla, we find that axonal responses of the different photoreceptor types become decorrelated (yR8 and pR8, yR7 and pR8) and in some cases, anti-correlated (pR7 and both R8s, yR7 and yR8).

The responses we measured at the level of photoreceptor outputs vary along two main axes: one that compares UV and visible wavelengths (y/pR7s and yR8), and one that compares blue with UV + green wavelengths (pR8). Can these two axes of opponency produce an efficient representation of the chromatic information detected at the retinal level? Inspired by the Buchsbaum and Gottschalk [5] study in humans, we used principal component analysis (PCA) to ask whether these axes preserve the chromatic information conveyed by R7 and R8 photoreceptors, while also decorrelating the inputs (Figure 5C–D). The first principal component (PC) is achromatic, with equal loading for all opsin types, and it accounts for over half of the variance. Higher PCs therefore describe variance in the chromatic domain. The second PC opposes the two R7 opsins and the two R8 opsins, corresponding to comparison between the UV and the visible parts of the spectrum (Figure 5E). The third PC opposes Rh5 and Rh3 + Rh6, which corresponds to a comparison between blue and UV + green (Figure 5F). The last PC opposes Rh3+Rh5 and Rh4+Rh6. The first two chromatic PCs together with the achromatic PC explain 97% of the variance. Interestingly, these two chromatic PCs broadly describe the two types of responses we measure at the output of R7 and R8: UV vs visible (observed in pR7/yR7 and yR8) and blue vs UV + green (observed in pR8) (Figure 5E–F). The first chromatic axis is supported by intra-ommatidial interactions, whereas the second chromatic axis necessitates inter-ommatidial interactions. Therefore, by aligning with these two axis, the opponent mechanisms we describe not only efficiently decorrelate chromatic signals, but also retains maximum chromatic information while reducing the overall dimensionality of the inputs.

A caveat of this analysis is that it assumes a flat spectrum, which does not take into account reflectances in naturalistic scenery. We therefore also explored a more biologically relevant context by performing the same analysis using a set of natural stimulus spectra, spanning the relevant wavelength range of fruit flies (300–600nm) (Figure S5A). In this case, PCA on all four opsin channels reveals similar principal components as in the case of a flat spectrum. This finding indicates that across conditions, our observed opponent responses are close to the optimal decorrelation of input signals using PCA (Figure S5B–C). This consistency across conditions fits with the idea that a purpose of this circuit is to remove correlation in the input signals which mainly arise from the overlap of the opsin sensitivities, rather than the composition of the spectrum.

A recurrent model of early color circuits predicts spectrally opponent R7 and R8 outputs

We next asked whether the circuit architecture we identified and tested experimentally can quantitatively reproduce the opponent responses we measure in R7 and R8 outputs. To inform the construction of our model, we first confirmed that photoreceptor axonal outputs are linear with regard to their calculated rhabdomeric inputs (i.e. log (q)) using two empirical measures of scalar invariance and additivity (see STAR methods; Figure S6A–F).

Because photoreceptors integrate inputs linearly, we first performed a linear regression without biological constraints. We used the calculated rhabdomeric responses as independent variables to fit our amplitude measurements (see STAR methods; Equation 11). We found that comparisons between measured axonal responses and estimated responses based on linear regression fall on the unity line (Figure S6G–J), thus providing a good fit (Figure 6A). The unconstrained linear regression provides a benchmark for our next model which includes biological circuit constraints.

We next built a linear recurrent network constrained by the circuit connectivity and synaptic signs (see STAR methods; Equation 12). The overall architecture of the network consists of direct inhibitory connections between photoreceptors within a single ommatidium, and indirect connections via the excitatory interneuron Dm9. Dm9 receives inhibitory inputs from all four photoreceptors and feeds back onto all photoreceptors. We fit the steady state of this model to our measured amplitudes (see STAR methods; Equation 14). When constrained by this architecture, our model has goodness-of-fits comparable to the unconstrained linear regression, even though the fully-parameterized recurrent model uses fewer parameters (Figure 6A). Our model also provides fitted tuning curves that closely approximate the opponency we observe in our data (Figure 6D). This shows that our proposed circuit is mathematically plausible given our measured responses, while also providing a biological constraint consistent with our experimental observations.

Finally, we aimed at further constraining the model by using synaptic counts obtained by EM reconstructions as a proxy for synaptic weights [23, 27]. To compare the performance of the different models, we calculated the Bayesian information criterion (BIC) (see STAR methods; Equation 17), which provides a metric that balances the overall error with the number of parameters in the model (a lower BIC value is preferred). The “parameter-free” model, which we refer to as the synaptic count model, qualitatively predicts our data, as seen in the tuning curves it produces (Figure 6D). However, it does not quantitatively perform as well as the fully parameterized model (Figure 6A, B). This is likely due to the fact that in this synaptic count model, we make the explicit assumption that the gains of the different neurons in the circuit are equal, which is not necessarily biologically plausible. We therefore fitted our data to a model that includes fitted gain parameters for each of the photoreceptors and Dm9 separately, keeping synaptic counts as synaptic weights for the connections between neurons. We refer to this as the synaptic count + gain model. The gain parameters we obtain are similar between photoreceptor types, and larger for Dm9 (Figure 6E). This model performs just as well as the fully parameterized model, both qualitatively and quantitatively (Figure 6A, B, D). As a control, we replaced the weights in our model with randomly drawn sample weights 10,000 times, and created a distribution of R^2 values (Figure 6C). We found that using the synaptic count for our weights results in a significantly

better performance than when using random weights. Therefore, the synaptic count data retrieved from EM gives a non-random estimate of input strength to photoreceptors.

We used our model to predict the full-field spectral filtering properties of each photoreceptor (Figure 6F). These filtering properties reflect our experimental tuning curves, but also predict the response of photoreceptors to arbitrary spectral distributions. In Figure 6G, we modeled the sensitivities of the center and the surround separately. We found that sensitivities in the center are in all cases bi-lobed, corresponding to comparisons between the UV part of the spectrum and the visible part, as expected. Additionally, we found that the sensitivities of the surround are broadband and strongest between 350 nm and 500 nm. The predictions made by our model lay the groundwork for future experiments in which spatially patterned stimuli can be used to further explore how this circuit processes information both spatially and spectrally.

Discussion

In this work, we report the spectral tuning of wavelength-specific R7 and R8 photoreceptor outputs in the visual system of the fruit fly *Drosophila melanogaster.* We find that each R7 and R8 output displays distinct spectrally opponent properties. These opponent signals are a consequence of a dual circuit: one that consists of reciprocal inhibition between R7 and R8 from the same ommatidum, enabling UV vs visible comparison at one point in space, and another that supports lateral inhibitory interactions between R7s and R8s from neighboring ommatidia, allowing for additional comparisons to be made in the spectral domain (e.g. blue vs green) between different points in space. We show that the latter is mediated by the horizontal-cell-like Dm9 neuron. A consequence of this dual circuit is an efficient decorrelation of photoreceptor signals, which reduces the dimensionality of the system while preserving maximum information. Our anatomically constrained linear recurrent model describes our findings and shows that synaptic count is a quantitative predictor of circuit function. We also predict the spatio-chromatic receptive field structure of each photoreceptor using our mathematical model.

Spectral opponency efficiently preserves chromatic information while decorrelating photoreceptor output signals

Theories of efficient coding postulate that the purpose of the early visual system is to compress redundant information and remove noise prior to neural transmission [28, 29]. Redundancy stems from correlations that occur extrinsically, in the statistics of natural scenes (chromatically, spatially and temporally), but also intrinsically, produced by the strong spectral overlap of photoreceptors' opsin sensitivities. One well-known way of removing these correlations is via a linear decomposition [5, 28, 29]. In accordance with this, we showed that the photoreceptor outputs of *Drosophila* perform a linear transformation on the inputs that orthogonalizes photoreceptor responses (decorrelation) and creates opposing, near-symmetric chromatic channels (strong anti-correlation). pR7/yR7s and yR8s compare the UV vs the visible part of the spectrum (all crossing over between 380–430 nm), forming near-mirror images of each other. pR8s are the only photoreceptors with a three-lobed sensitivity, comparing blue to both UV and green. Using PCA analysis,

we found that these axes of opponency efficiently remove correlation in incoming signals resulting from overlapping opsin sensitivities, and effectively reduce the dimensionality of the encoding space, while maximally preserving spectral information. In other words, the transformation we describe, from four photoreceptor channels to two opponent axes, allows for a nearly full reconstruction of chromatic information. Achromatic information is likely encoded in neural pathways downstream of R1–6. However, spectral decorrelation and dimensionality reduction are likely not the only goals, as pR7, yR7, and yR8 photoreceptors all encode spectral inputs along the UV-vs-visible axes. The absolute value of the correlation coefficients of pR7-yR8 and yR7-yR8 outputs are actually larger than the absolute value of their predicted correlation coefficients at the level of the retina. Such redundancy may serve to deal with noise in the system, so that visual stimuli along the UV-vs-visible axis can be robustly encoded [30]. This circuitry could effectively support behaviors that depend on differences between short and long wavelengths.

A circuit constrained recurrent model predicts R7 and R8 spectrally opponent outputs with complex spatio-chromatic receptive fields

By building an anatomically constrained model of the underlying circuit, we showed that the circuit architecture we identify can quantitatively produce the signals we measure at the level of R7 and R8 outputs. We further constrained our model using synaptic counts obtained from EM. Synaptic count data has been previously used to gain intuition about which inputs to a given neuron are likely strongest [31]. However, it was not clear whether synaptic count could be used more quantitatively to predict function. Using our model, we showed that synaptic count is both a good qualitative and quantitative estimate of synaptic strength. This result demonstrates that, at least in this type of hard-wired sensory circuit, synaptic count provides useful information for understanding circuit function.

We used our biologically constrained model to make predictions of the responses of photoreceptor outputs to untested visual stimuli. Our model predicts that the result of this dual opponent system is a spatio-chromatic receptive field for each photoreceptor output with a UV vs visible color-opponent center and an antagonistic achromatic surround (Figure 6G). The size of the center is predicted to correspond to one ommatidial angle, or ≤ 5 degrees [32, 33]. The size of the surround is likely determined by the columnar extent of the horizontal cell Dm9, which has been found to span on average 7 columns [24], corresponding to 35 total degrees in visual space (with a width of ~ 15 degrees). Due to the limitations of our current visual stimulus system, which only allows for full field stimuli to be presented, these receptive fields were not tested experimentally. Moving forward, a patterned chromatic visual stimulus will enable direct measurements of receptive field sizes and spectral properties, and enable testing of the predictions of our model. Finally, our model does not capture the temporal dynamics of the responses we measure, as we were restricted by the kinetics of our indicator. Further experiments with better time resolution will allow for exploration of both center versus surround and chromatic versus achromatic dynamics - both of which are important features to consider in terms of signal processing and behavioral consequences.

Functional implications

The Dm9-mediated, inter-ommatidial circuit that we describe here can be directly compared to mechanisms that establish opponency in the retina of trichromatic primates. There, midget cells compare photon catches between M and L cones, creating a red-green opponent axis. This opponent channel is thought to be established through non-selective wiring of H1 horizontal cells with M and L cones ([34, 35]; but see [36]). In the fovea, each midget ganglion cell receives inputs from a single M or L cone at its center, and a mixture of M and L cones in its surround. This so-called “private line” circuitry supports both high acuity and cone opponency, resulting in multiplexed signals capturing both high-resolution achromatic stimuli that isolate the center and low-spatial resolution chromatic stimuli that engage both center and surround [37, 38]. The ambiguity between these multiplexed signals may be resolved by differential processing at the level of downstream pathways, which may preserve either chromatic signatures at the expense of spatial information, or vice versa ([39], but see [40]).

The circuit we describe at the level of photoreceptor outputs is similar to the foveal midget pathway: it is horizontal-cell-mediated, samples the center at one point in space, samples the surround randomly from the distribution of opsins in the eye, and creates spatially and spectrally opponent responses. Like the midget pathway, R7 and R8 photoreceptor signals also convey multiplexed information, which could be differentially processed downstream. However, a key difference in flies is that the center itself is spectrally opponent, and therefore, signals in the fruit fly would be separated into a high-resolution chromatic pathway and a low-resolution chromatic pathway. A separate high-resolution achromatic pathway also exists in flies, driven by R1–6, which are active in daylight. Flies have been shown to discriminate between blue and green large areas of illumination [7, 9] but it remains to be seen whether they take advantage of their capacity for spatially acute color vision behaviorally, as swallowtail butterflies do (*Papilo xuthus*) [41], but not honeybees (*Apis mellifera*) [42, 43].

Unlike the simple eye of mammals, the compound eye of the fly is not subject to the limitations of optical aberration. It thus has the capacity to build a chromatic comparison system that operates at the full resolution of the eye, equivalent to the resolution of achromatic pathways. It uses an insect specific circuit architecture that is well suited to extract chromatic information for small target visual stimuli, at a scale equivalent to the resolution of the fly eye (~ 5 degrees). Additionally, the fly uses a horizontal-cell-mediated circuit based on lateral interactions, similar to the one used in primates. This system allows for further chromatic comparisons to be made, like the one we measured between the blue and green parts of the spectrum, and is also well tuned to extract chromatic information for large target visual stimuli. Overall, the dual circuit combines an insect specific circuit motif, which could enable chromatic vision at the full resolution of the fly eye, and an evolutionarily convergent center-surround circuit motif, which could allow for lower spatial resolution chromatic vision with extended spectral resolution.

STAR Methods

LEAD CONTACT AND MATERIALS AVAILABILITY

Further information and requests for resources and reagents should be directed to and will be fulfilled by the Lead Contact, Rudy Behnia (rb3161@columbia.edu). Fly strains used in this study will also be available upon request.

EXPERIMENTAL MODEL AND SUBJECT DETAILS

Fly Genetics—w+ flies were reared on standard molasses-based medium at 25°C - 28°C. The rhodopsin drivers used for imaging photoreceptors Rh3-Gal4 and Rh6-Gal [46] along with Rh1-Gal4, Rh4-Gal4 and Rh5-Gal4 [47] were expressed heterozygously along with 20X-UAS-GCaMP6f, also expressed heterozygously (Bloomington stock center: 52869). Dm9 cells were targeted for imaging, staining and silencing using both the R21A12-Gal4 or the R32E04-Gal4 drivers (Bloomington stock center: 48925 and 49717). Silencing was performed using UAS-Kir2.1 constructs (made and gifted by by Daisuke Hattori), and imaging with Rh5-LexA [48] (gift from Claude Desplan) and LexAop-GCaMP6f (BL44277). Phototransduction rescue experiments were performed using *norpa-* and UAS-NorpA1 or UAS-NorpA2 constructs [16] (gifts from Mathias Wernet). Ort rescue experiments were performed in a $hiscl^{134}$ ort^{1} background (gift from Mathias Wernet), heterozygous with $hiscl^{134}$ ort^{1} cry^{02} [49] by also expressing a UAS-ort construct [49] (both gifts from Francois Rouyer). For immunostaining, UAS-mCD8 (gift from Claude Desplan) or UAS-GCaMP6f (Bloomington stock center: BL42747) constructs were used to label cell types of interest. For clones, hs-FLPG5.PEST and 10XUAS(FRT)myr::smGdP-V5/FLAG/HA-10XUAS(FRT) constructs were used (Bloomington Stock center 64085) as well as Rh4-LacZ [50] (Gift from Claude Desplan). For optogenetic imaging, Dm9 cells were targeted with the R32E04-LexA driver (Bloomington stock center: BL54739), and the 13X-LexAop2-IVS-Syn21-Chrimson-tdTomato-3.1 construct (gifted by Barret Pfeiffer, Allan Wong and David Anderson). R7 photoreceptors were simultaneously imaged using a panR7-Gal4 driver (gift from Claude Desplan). Control flies expressed both panR7-Gal4 and UAS-GCaMP6f constructs, but were missing either the R32E04-LexA driver or the 13X-LexAop2-lVS-Syn21-Chrimson-tdTomato-3.1 construct. All flies for optogenetic imaging were *norpa-* mutants.

METHOD DETAILS

Two-Photon Calcium Imaging—Imaging was conducted with a two-photon microscope (Bruker) controlled by PrairieView 5.4 and a mode-locked, dispersion compensated laser (Spectraphysics) tuned to 930 nm. We imaged with a 20x water-immersion objective (Olympus XLUMPLFLN, 1.0 numerical aperture). In front of the photomultiplier tube (Hamamatsu GaAsP), we mounted a band-pass filter (Semrock 514/30 nm BrightLine) to reduce bleed-through from the visual stimulus setup. T-Series were acquired at 15–30Hz and lasted for a maximum of eight minutes with each frame at x-y imaging being 145×90 pixels.

All experimental animals for functional imaging were briefly anaesthetized using carbon dioxide on the day of eclosion, and imaged at ages ranging from 3–13 days. Flies were prepared for two-photon imaging based on methods previously described [51]. Flies were

anesthetized using ice, and mounted in a custom stainless-steel/3D-printed holder. A window was cut in the cuticle on the caudal side of the head to expose the medulla, where the axons of photoreceptors could be imaged. The eyes of the of the fly remained face down under the holder, and remained dry while viewing the visual stimuli, while the upper part of the preparation was covered with saline. The saline composition was as follows (in mM): 103 *NaCl*, 3 *KCl*, 5 *n – tri*(*hydroxymethyl*)*methyl*– 1*Aminoethane – sulphonicacid*, 8 *trehalose*, 10 *glucose*, 26 $NaHCO_3$, 1 NaH_2PO_4, 1.5 $CaCl_2$, and 4 $MgCl_2$, adjusted to 270mOsm. The pH of the saline was equilibrated near 7.3 when bubled with 95% O_2 / 5% CO_2 and perfused continuously over the preparation at 2 *ml* / *min*. The imaging region of interest was limited to the region of the medulla photoreceptors are directly activated by stimuli. Specifically, the z-depth was zeroed at the same level for each fly (the dorsal part of the medulla) and photoreceptor responses were measured from 50–90 microns below that point. Responses were measured from the rostral fourth of the medulla in that plane. The dorsal third of the eye was covered with black acrylic paint to avoid the region where Rh3 and Rh4 are coexpressed in R7s [52]. Calcium responses were stable throughout imaging.

Flies used in optogenetic experiments were reared in the dark on fly food supplemented with all trans-Retinal (1mM, Sigma-Aldrich #R2500). 7–8 day old flies were imaged under the two-photon microscope in the *in vivo* preparation configuration described previously. Light activation of the Chrimson ion channel was achieved with a 660nm LED (Thorlabs M660L4) fit with a long pass filter (Thorlabs, 10LWF-400-B). The LED was mounted directly above the preparation and delivered at 33Hz light pulses of 0.195 mW/(mm^2) irradiance for a duration of 1 second. Image acquisition was continuous during light activation. Light pulses were repeated 10 times with 30 second intervals between. The expression of the Dm9 driver was verified after each imaging session by viewing td-Tomato excited at 1020nm.

Immunohistochemistry—Immunostainings were done as described by Morante and Desplan [53] with some modifications. Adult flies were anesthetized on ice. Brains were dissected in PBS and fixed in 4% formaldehyde for 35 minutes on ice. Brains were incubated at 4°C overnight with the following primary antibodies: sheep anti-GFP (1:500, AbD Serotec), rat anti-DN-cadherin (1:50, DSHB) and mouse anti-chaoptin (1:50, DSHB) diluted in PBST (0.3% TritonX-100 in PBS). Secondary antibodies were incubated for 2 hours at room temperature. Images were acquired using an Nikon A1R Confocal Microscope.

To obtain Dm9 clones, 2–3 day old flies were heat shocked for 3 minutes at 39°C and dissected 2 days later. Dm9 clones were labeled with the FLAG epitope tag using the primary antibody rat anti- DYKDDDDK (1:200, NBP1). Yellow R7 photoreceptors were labeled with an Rh4-LacZ reporter construct and the primary antibody rabbit anti-beta-galactosidase (1:2000, MBP).

Visual Stimulation

Hardware: We produced full-field wavelength-specific stimuli using a customized setup (Figure 1C). The setup consists of six LEDs in the UV and visible wavelength range

(ThorLabs M340L4 - dUV/340nm; M365L2 - UV/360nm; M415L4 - violet/415nm; M455L3 - blue/455nm; M565L3 - lime/565nm; M617L3 - orange/615nm). A customized driver drove the five LEDs from dUV to lime. These LEDs turned on during the return period of the x-scanning mirror in the two-photon microscope (fly-back stimulation). We used the TTL signal generated by the two-photon microscope at the beginning of each line-scan of the horizontal scanning mirror (x-mirror) to trigger the LED driver. An individual T-Cube (Thorlabs LEDD1B T-Cube) drove the orange LED. Stimuli were generated using customized software written in Python. The update rate for the LED voltage values was 180Hz.

The different light sources were focused with an aspheric condenser lens (ThorLabs ACL2520U-A) and aligned using dichroic mirrors (dUV-UV dichroic - Semrock LPD01-355RU; UV-violet dichroic - Semrock FF414-Di01; violet-blue dichroic - Semrock Di02-R442; blue-lime dichroic - Semrock FF495-Di03; lime-orange dichroic - Semrock FF605-Di02). The collimated light passed through a diffuser (ThorLabs DG10-1500A) before reaching the eye of the fly, which is positioned 2cm away.

Intensity calibration: In order to measure the intensity of our LEDs across many voltage outputs, we used a photo-spectrometer (250–1000 nm, Ocean Optics) that was coupled by an optic fiber and a cosine corrector and was controlled using our customized Python software. The photo-spectrometer was mounted on a 3D printed holder that was designed to fit on our experimental rig and approximately aligned with the fly's point of view. For each LED, we tested a total of 40 voltage values (linearly separated) from the minimum voltage output to the maximum voltage output. For each voltage value tested, we adjusted the integration time to fit the LED intensity measured, and averaged over 20 reads to remove shot noise.

Using the spectrometer output, we calculated the absolute irradiance ($I_p(\lambda)$; in W/m^2m) across wavelengths using the following equation:

$$I_p(\lambda) = C_p(\lambda)\frac{S_p(\lambda) - D_p(\lambda)}{\Delta t \cdot A \cdot 100} \quad (1)$$

where $C_p(\lambda)$ is the calibration data provided by Ocean Optics ($\mu J/count$), $S_p(\lambda)$ is the sample spectrum ($counts$), $D_p(\lambda)$ is the dark spectrum ($counts$), Δt is the integration time (s), and A is the collection area (cm^2).

Next, we converted absolute irradiance to photon flux (E_q; in $\mu E/nm$):

$$E_p(\lambda) = \frac{I_p(\lambda) \cdot c \cdot \lambda}{h \cdot N_A \cdot 10^6} \quad (2)$$

where $\frac{h \cdot c}{\lambda}$ is the energy of a photon with h as Planck's constant ($6.63 \cdot 10^{-34}\ J \cdot s$), c as the speed of light ($2.998 \cdot 10^8\ m/s$), and λ the wavelength (nm). N_a is Avogadro's number ($6.022 \cdot 10^{23}\ mol^{-1}$).

Stimulus Design: Each stimulation protocol had 10–20 seconds before and after the stimulation period in order to measure baseline fluorescence (fluorescence to background light). Because we anticipated measuring opponent waveforms at the level of photoreceptor outputs, we used single wavelength dominant backgrounds (UV for R7s and blue for R8s), which have the advantage of highlighting opponent signals (Figure 2, 3, S2, 4I–J, and S3C–D). In these conditions, GCaMP6f fluorescence was increased at baseline, allowing decreases to be readily measured.

For the correlation analysis, PCA, and modeling, we acquired an additional dataset of spectral tuning measurements, in which measurements for all photoreceptor types were made with the same stimulus over a large range of intensities and combinations of single wavelengths (Figure 5, 6, S4, and S6). We used a background with a flat spectrum at an intensity of 10 μE with luminant multiples ranging over several orders of magnitude (Figure S1). The opponent waveforms we measure under these conditions are consistent with our wavelength-dominant background experiments (compare Figure 2F–M to Figure S4). For Dm9 recordings, we also used the flat spectrum (Figure 4E–H).

The intensities of each LED for the different background conditions are shown in Table S1. Flies were adapted to the different background lights for approximately 5 minutes before the start of the recording. For the flat background condition, we chose the intensities of the LEDs by fitting the following equation:

$$\min\left\{\|\mathbf{Lx}-\mathbf{b}\|^2, \mathbf{l}\le\mathbf{x}\le\mathbf{u}\right\} \tag{3}$$

where **L** is a matrix of the normalized LED intensities across wavelengths (each row is a different wavelength and each column is a different LED), **x** is a vector of corresponding LED intensities to fit, and **b** is the background spectrum across wavelengths (i.e. a flat spectrum with an overall intensity of 10 μE). **x** is bounded by the minimum **l** and maximum **u** intensity each LED can reach. The minimum intensity is zero for all LEDs, and the maximum intensities are (in μE): dUV - 11.7, UV - 21.7, violet - 17.0, blue - 16.4, lime - 18.7, and orange - 145.1.

We wanted to show different single Gaussian wavelengths between 320–620 nm with a standard deviation of 10 nm on top of our background (i.e. add these single wavelengths to our background light) (Figure 1F). We also wanted to show these single wavelengths across different intensities. To do this, we built a simple model of opsin photon capture.

The absolute photon capture of an opsin (i.e. the number of photons absorbed) given any spectral stimulus at a specific intensity can be calculated as follows [17, 18]:

$$Q_i = C_i \int S_i(\lambda) I(\lambda) d\lambda \tag{4}$$

where Q_i is the absolute photon capture of opsin i, C_i is the absolute sensitivity of opsin i, S_i is the relative spectral sensitivity of opsin i, and I is the spectrum of light entering the eye. Equation 4 implies that the identity of a photon is lost upon absorption by a photoreceptor (i.e. the principle of univariance). As the scaling factor C_i is usually unknown, the relative

photon capture can be calculated instead assuming von Kries chromatic adaptation [18, 54, 55]:

$$q_i = \frac{Q_i}{Q_i^b} \tag{5}$$

where q_i is the relative photon capture of opsin i, and Q_i^b is the absolute photon capture of opsin i for the background illuminant.

For our six LEDs, we can calculate the normalized relative capture across the fly opsins:

$$\mathbf{A} = \mathbf{SL} \oslash \mathbf{p} \tag{6}$$

where **A** is a matrix corresponding to the relative photon capture of each opsin for each LED (*opsin* × *LED*), S is a matrix of the relative spectral sensitivities for all opsins across wavelengths (*opsin* × *wavelength*), **L** is a matrix of the normalized LED intensities across wavelengths (*wavelength* × *LED*), and **p** is a vector of the absolute capture for all opsins for the background spectrum. ⊘ signifies element-wise division.

To emulate our desired stimuli using our six LEDs, we first calculate the relative photon capture of each opsin present in the fly eye given the desired stimulus. This gives us a vector **q**. Given **A** from equation 6, we find the optimal intensities for each LED to match our desired **q** as follows:

$$\min\left\{\|\mathbf{w} \odot (f(\mathbf{Ax}) - f(\mathbf{q}))\|^2, \mathbf{l} \leq \mathbf{x} \leq \mathbf{u}\right\} \tag{7}$$

where **x** is a vector of corresponding LED intensities to fit, w is a weighting factor for each opsin, and f is a link function (i.e. the identity for the single wavelength dominant backgrounds and the log for the flat background). The weighting factor w was 1 for all opsins in the case of the single wavelength dominant backgrounds, and 1 for all opsins, except 0.1 for Rh1, in the case of the flat background. The lower (**l**) bound on **x** corresponds to the background intensity of each LED, as we desired to add a spectrum on top of the background. The upper (**u**) bound on **x** correspond to the maximum intensity each LED can reach. ⊙ signifies element-wise multiplication.

We used a total of three stimulus sets. The accuracy of our fitting procedure is shown in Figure S1G–R. Each individual stimulus (i.e. each simulated wavelength or wavelength mixture) lasted 0.5 seconds with a 1.5 second period between stimuli. The background intensity values are shown in Table S1. Our UV-dominant and blue-dominant background was used to test the existence of color opponency in R7s and R8s, respectively. Both stimulus sets had a total of 16 wavelengths that were tested spanning 320 to 620 nm, and each stimulus was repeated three times. In the case of the UV-dominant background, each wavelength was fitted using an intensity that was 5 times bigger than the total background intensity (i.e. a luminant multiple of 5). In the case of the blue-dominant background, the wavelengths were a luminant multiple of 15. In the case of the UV-dominant background, we discarded the simulated wavelengths 480, 500, and 520 nm, because the dUV LED is on

for these longer fitted simulated wavelengths; the algorithm was trying to fit the relative capture of the broadband rh1 opsin (Figure S1A, G, M). In the case of the blue-dominant background, we discarded the wavelengths 360 and 440 nm, because the green and orange LED is on respectively for these shorter fitted simulated wavelengths; the algorithm was trying to fit the relative capture of the broadband Rh1 opsin (Figure S1B, H, N). To avoid this issue during fitting of the flat background stimuli, the error for the Rh1 capture is weighted differently (Equation 7). This is reasonable considering R1–6 photoreceptors do not contribute significantly to R7 and R8 photoreceptor responses (Figure S2I–P).

For the flat background our single wavelengths included: 320 nm, 340 nm, 360 nm, 380 nm, 400 nm, 420 nm, 440 nm, 460 nm, 500 nm, 530 nm, 570 nm, 620 nm. We tested luminant multiples of 0.2, 1, 4, and 8. We also mixed the wavelengths 340 nm and 440 nm, 380 nm and 620 nm, 320 nm and 530 nm, 460 nm and 570 nm, and 400 nm and 570 nm. As predicted, putative rhabdomeric responses correspond to the log of the relative photon capture (Figure 2B–E), we mixed wavelengths in the following way to test for linearity:

$$\begin{aligned} \log(\mathbf{q}_{mix}) &= p\log(\mathbf{q}_{wl1}) + (1-p)\log(\mathbf{q}_{wl2}) \\ \mathbf{q}_{mix} &= \mathbf{q}_{wl1}^{p} \cdot \mathbf{q}_{wl2}^{1-p} \end{aligned} \tag{8}$$

where $\mathbf{q}_{mix}$ is the calculated relative capture for the mixture of wavelengths, p is the proportion of wavelength $wl1$, $\mathbf{q}_{wl1}$ is the calculated capture of wavelength wl1, and $\mathbf{q}_{wl2}$ is the calculated capture of wavelength $wl2$. Using Equation 7, we fit the calculated captures for the mixture of wavelengths, as we did for the single wavelengths. For testing linearity of our responses, we used the mixtures at the luminant multiple of 1, as it provided good fits in our regression (see Figure S1D, J, P, S–W) and large calcium responses (see Figure S4 and Figure S6B–F).

For any analysis and modeling work, we used the calculated relative capture after fitting and not the target relative capture, we were aiming to simulate.

Quantification of Imaging Data—All data analysis for *in vivo* calcium imaging was performed in Python using custom-made Python code and publicly available libraries. To correct our calcium movies for motion we performed rigid translations based on template alignment using the algorithm provided by the CaImAn package [56]. As a template for rigid motion correction, we used the average projection of the first ten seconds of every calcium movie during which we did not show any visual stimuli.

Image Segmentation: Region of interestes (ROIs) were selected automatically using a custom-made approach and verified manually. A standard deviation projection was taken of the complete image stack. We thresholded the projected image in three ways to identify pixels that are certainly part of a ROI, certainly part of the background, and possibly part of a ROI. These thresholded images were used to identify connected components (i.e. individual ROIs). Next, we applied a watershed transformation to obtain the individual ROIs. We discarded any ROIs of fewer than 5 pixels.

Signal Extraction: To extract calcium traces from our segmented images, we first took the average fluorescence of each ROI at each time point. We subtracted the mean background fluorescence - the mean fluorescence of all pixels that do not belong to any ROI - from each trace to remove background noise. To calculate the dF/F signal, we use as a baseline for our denoised traces the 5th percentile of a rolling 30 second time window. Finally, we smooth our dF/F signal with a Gaussian filter of size 0.32 seconds and a standard deviation of 0.08 seconds. We discarded ROIs, where the signal-to-noise (SNR) ratio was smaller than 1.5. The SNR was defined as the standard deviation of the signal during stimulation over the standard deviation of the signal before and after the start of stimulation ($SNR = \sigma_{stim}/\sigma_{baseline}$).

Peri-stimulus time histograms (PSTHs): dF/F traces were aligned to the stimulus start times and averaged for each ROI. Amplitude measurements were taken on these averaged PSTHs for each ROI. As each stimulus was 0.5 seconds long amplitudes were calculated by taking the average dF/F response between 0.42 and 0.5 seconds after the stimulus onset and subtracting the average dF/F response 0.15 to 0.05 seconds before stimulus onset (i.e. the baseline). The max-dF/F signal of the spectral tuning curves was calculated by dividing the mean across all ROIs of the wavelength with the maximum response.

Signal sorting: In the case of the double NorpA rescues, we needed to sort our individual ROIs. To do this, we fitted the data to the log of the relative photon capture of the opsin each photoreceptor expresses. For example, in the case of the pR8 and yR8 NorpA rescues, we fitted each ROI to the log of the relative photon capture of Rh5 and Rh6 separately. Next, we assigned each ROI to the cell type according to which fit explained more of the variance. In our example, if the Rh5 fit is better than the Rh6 fit for a ROI, that ROI is a putative pR8 axon.

Correlation and Principal Component Analysis

Correlation Coefficients: To calculate the correlation coefficients of actual and predicted responses, we first calculated the covariance matrix ($\mathbf{\Sigma}$). We calculated the covariance as follows:

$$\mathbf{\Sigma} = \mathbf{Y}^T\mathbf{Y} \tag{9}$$

where $\mathbf{Y}$ are the responses of the different cell types across stimuli ($stimulus \times cell - type$).

We calculate the correlation coefficient matrix ($\mathbf{C}$), as follows:

$$\mathbf{C} = \frac{\mathbf{\Sigma}}{\sqrt{diag(\mathbf{\Sigma})diag(\mathbf{\Sigma})^T}} \tag{10}$$

Decomposition of retinal inputs: To obtain principal components of our retinal inputs, we first calculated the covariance matrix ($\mathbf{\Sigma}$). In the case of a uniform Fourier frequency power spectrum (flat stimulus spectrum), we calculated the covariance using the spectral sensitivities of each opsin, similar to Buchsbaum and Gottschalk [5]. We used the log-plus-

one transformed spectral sensitivity for our covariance calculation to account for our observation that the retinal response is proportional to the log of the relative photon capture. This log-plus-one transformation had a negligible effect on the actual principal components obtained. In the case of the hyperspectral reflectance dataset, we first calculated the relative photon capture of each opsin for each reflectance and applied a log transformation. The covariance was calculated on this dataset as in Equation 9.

In order to decompose the opsin spectral sensitivities, we simply eigendecompose the covariance $\mathbf{\Sigma}$ to obtain eigenvalues and eigenvectors. This is equivalent to principal component analysis (PCA), where the eigenvectors correspond to the different components and the eigenvalues are proportional to the explained variance for each component. To construct principal component tuning curves, we took the dot product of the photoreceptor inputs (*stimulus* × *opsin*) and the eigenvectors (*opsin* × *component*).

PCA on segregated pale and yellow pathways: We also compared our complete PCA analysis of the hyperspectral dataset to the decomposition of inputs along a segregated pale and yellow columnar organization [6], corresponding to intra-ommatidial interactions alone; i.e. performing PCA on the pale and yellow inputs separately (Figure S5D). The two chromatic components obtained this way are, somewhat trivially, still correlated, as only retinal inputs from the same type of ommatidium are decomposed (Figure S5E–F). Due to the large overlap of the spectral sensitivities between pale and yellow photoreceptors, these two separate chromatic components have a correlation coefficient of 0.6. This indicates that having two separate chromatic pathways (that just rely on intra-ommatidial connections) creates an inefficient representation of the color space available to the fly. Instead, the circuit we describe, combining both intra- and inter-ommatidial interactions, displays more complete opponent mechanisms at the early photoreceptor level than previously thought, and is also capable of efficient encoding and transmission of chromatic information.

Hyperspectral Reflectance Dataset: We obtained the hyperspectral reflectance dataset from http://www.reflectance.co.uk [57, 58, 59, 60, 61]. The obtained hyperspectral reflectances and the opsin sensitivities were linearly interpolated between 300 and 600nm to calculate the relative photon capture. The dataset mostly contains a variety of flower reflectances. While flowers are not known to be of relevance in *Drosophila* ecology, we argue that in general, natural reflectances in defined wavelength ranges are very similar, and thus comparable for purposes of decomposition [62].

Modeling

Linearity of the system: We asked if photoreceptor axonal outputs are linear with regard to their calculated rhabdomeric inputs (i.e. log (q)). For this analysis, we acquired an additional dataset of spectral tuning measurements, in which measurements for all photoreceptor types were made with the same stimulus over a large range of intensities(Figure S4). We used a background with a flat spectrum at an intensity of 10 μE with luminant multiples ranging over several orders of magnitude (Figure S1). The opponent waveforms we measure under these conditions are consistent with our previous experiments. To test for linearity, we assessed two empirical measures: scalar invariance and additivity. The estimated zero-

crossing points of the opponent tuning curves of R7s/R8s do not significantly change at different intensities of light measurements, showing scalar invariance within the bounds of our recording conditions (Figure S6A). To test for additivity, we measured the responses of photoreceptor outputs to wavelengths mixed in different ratios (see STAR methods; Equation 8) and compared the responses to corresponding linear additions of the single wavelength responses. Figure S6B–F shows the results for mixtures between 340/440 nm, 380/620 nm, 400/570 nm, 460/570 nm, and 320/530 nm at four different mixing ratios. The measured responses to the mixtures (filled circles) do not significantly differ from the linear predictions (shaded area). Therefore, the circuit under investigation behaves linearly within the range of stimuli used in this study.

Linear Regression: To assess chromatic tuning of our responses, we fit a linear regression model to our data:

$$\mathbf{r} = \mathbf{X}\boldsymbol{\beta} \tag{11}$$

where **r** is the average amplitude response of a neuron type to the various stimuli in the flat background condition, **X** is the input space (i.e. the $\log(q)$ for each stimulus), and β are the associated weights for each input feature. Fitting was performed using 4-fold cross-validation. To improve numerical stability during the fitting procedure without biasing the end result, fitting was performed on a “whitened” input space (PCA whitening). After fitting, parameters were transformed back into “unwhitened” space. In order to assess goodness of fit for the different inputs, we calculated the 4-fold cross-validated R^2 values for each input space.

Linear regressions that include intra-ommatidial R7/R8 opsin pairs together with at least one additional opsin type provide better fits than when exclusively considering intra-ommatidial R7/R8 opsin pairs as independent variables (Figure S6K–N). This is most obvious in the case of pR7 and pR8. These regressions are consistent with findings that both intra- and inter-ommatidial interactions shape opponent responses in R7/R8.

Circuit Modeling: Given the hypothesized circuit architecture, we built a linear recurrent model described by the following equations:

$$\tau_{\mathbf{r}}\frac{d\mathbf{r}}{dt} = -\mathbf{r} - \mathbf{W}\mathbf{r} + \mathbf{y}_e e + \log(\mathbf{q}) \tag{12}$$

$$\tau_e\frac{de}{dt} = -e - \mathbf{y}_\mathbf{i}^T\mathbf{r} \tag{13}$$

where **r** is a vector of the responses of the photoreceptor axons, **W** is the connectivity matrix for the direct inhibitory connections, τ is the time constant, $\mathbf{y}_e$ is a vector of the synaptic weight from Dm9 back to each photoreceptor, e is the response of Dm9, **q** is the relative photon capture, $\mathbf{y}_i$ is the synaptic weights from the photoreceptors to Dm9. All weights are positive, and the inhibitory or excitatory nature of the synapse is indicated by the sign.

We can simplify the above equation by setting $\frac{de}{dt} = 0$, $\frac{d\mathbf{r}}{dt} = 0$ (i.e. steady-state condition), so that:

$$\left(\mathbf{I} + \mathbf{W} + \mathbf{y_e}\mathbf{y_i}^T\right) \cdot \mathbf{r} = \log(\mathbf{q}) \tag{14}$$

where **I** is the identity matrix. Using Equation 14, we fit the model to all our flat background data using least-squares and cross-validated our fits 4-fold.

The EM synaptic count proportions, we used, are in Table S2 [21, 23]. To normalize synaptic counts, we divided the synaptic count by the total number of synapses for each neuron. To change the gains of individual neurons using these fixed weights (synaptic count + gain model), we fit the Dm9 gain c and the photoreceptor gains **a** in the following equation using least squares:

$$\left(\mathbf{I} + \mathbf{W} + c \cdot \mathbf{y_e}\mathbf{y_i}^T\right) \cdot (\mathbf{a} \odot \mathbf{r}) = \log(\mathbf{q}) \tag{15}$$

We used our synaptic count + gain model fits for our prediction of the spectral filtering curve and center-surround receptive field. The spectral filtering curve is the predicted response to individual narrow single wavelengths (instead of broader single wavelengths which we were able to test). The center-surround receptive field was normalized to each peak response. The center corresponds to the predicted response, when removing the Dm9 interneuron ($center = (\mathbf{I} + \mathbf{W})(\mathbf{a} \odot \mathbf{r})$). The surround corresponds to the response to the input of each photoreceptor receives from Dm9 ($surround = c \cdot \mathbf{y_e}\mathbf{y_i}^T \cdot (\mathbf{a} \odot \mathbf{r})$).

Fitting for Spectral Sensitivities: We obtained the spectral sensitivities for the opsins Rh3, Rh4, Rh5, and Rh6 from Salcedo et al. [44]. We fit the raw sensitivities to the following equation [45]:

$$\begin{aligned} S(\lambda) = (e^{69.7 \cdot \left(0.8795 + 0.0459e^{-\left(\lambda_{max} - 300\right)^2/11940} - \frac{\lambda}{\lambda_{max}}\right)} \\ + e^{28 \cdot \left(0.922 - \frac{\lambda}{\lambda_{max}}\right)} \\ + e^{-14.9 \cdot \left(1.104 - \frac{\lambda}{\lambda_{max}}\right)} \\ + 0.674) \end{aligned} \tag{16}$$

where λ is the wavelength, λ_{max} is the peak wavelength, and S is the fitted spectral sensitivity.

QUANTIFICATION AND STATISTICAL ANALYSIS

The statistical details of each experiment can be found in the figure legends. For all PSTHs and tuning curves, we show the empirically-bootstrapped 95% confidence interval to indicate significance. To obtain these intervals, we randomly resampled from our data (independently across all ROIs) 1000 times and recalculated the mean. Next, we took the 2.5% and 97.5% percentile of our 1000 samples.

We fitted the various linear models using 4-fold cross-validation, and averaged over fits to obtain the cross-validated R^2 value.

We calculated the Bayesian Information Criterion (BIC) as follows:

$$BIC = n\ln(r/n) + k\ln(n) \tag{17}$$

wheren n is the number of data points, r is the sum of the squares of residuals (deviations predicted from actual empirical values of data), and k is the number of parameters in the model.

To assess significance of the synaptic count + gain model, we randomly drew weights and refit the model to obtain a null distribution. We used the same Equation 15 for fitting, and pulled random weights from a uniform distribution ranging from 0 to 1. Before fitting, the weights were normalized the same way the EM weights were normalized. We sampled a total of 10000 random weights to build a null distribution of the cross-validated R^2 values.

DATA AND CODE AVAILABILITY

We used common scientific Python packages for data management, analysis and modeling work, including numpy, scipy, matplotlib, sklearn, DataJoint [63], opencv, and, lmfit. Custom code related to calcium signal extraction is accessible on GitLab (https://gitlab.com/rbehnialab/colorvisionpaperl). The source code used for visual stimulation is available on GitLab (https://gitlab.com/rbehnialab/motyxia2). Raw data supporting the current study have not been deposited in a public repository because of their large size, but are available from the Lead Contact, Rudy Behnia (rb3161@columbia.edu). Modeling code is also available upon request.

Supplementary Material

Refer to Web version on PubMed Central for supplementary material.

Acknowledgments

We benefited from helpful conversations with L. Abbott and T. Movshon. We thank L. Abbott, C. Desplan and C. Zuker for comments on the manuscript. We thank M. Reiser for sharing data prior to publication, L. Zipusky for advice on Dm9 Gal4 lines, B. Pfeiffer A. Wong, D Anderson, F. Rouyer, D. Hattori and M. Wernet for fly stocks, D. Peterka for advice on imaging, R. Hormigo for help with the fly back system. RB was supported by NIH R01EY029311, the McKnight Foundation, Grossman Charitable Trust, the Pew Charitable Trusts and the Kavli Foundation. SLH acknowledges support from NSF GRF DGE-1644869 and NIH F31EY030319. MPC acknowledges support from NIH 5T32EY013933-19. JRK was supported by NIH F31EY029592. MPC, EO and MSW and this project were supported by NIH R01EY029311.

References

1. Rushton WAH, Review lecture. Pigments and signals in colour vision, J Physiol 220 (1972) 1P–31P. [PubMed: 5059236]
2. Shevell S, Martin P, Color opponency: A tutorial, J. Opt. Soc. Am. A 34 (2017) 1099–1108.
3. Su C-Y, Menuz K, Reisert J, Carlson JR, Non-synaptic inhibition between grouped neurons in an olfactory circuit, Nature 492 (2012) 66. [PubMed: 23172146]
4. Conway BR, Chatterjee S, Field GD, Horwitz GD, Johnson EN, Koida K, Mancuso K, Advances in Color Science: From Retina to Behavior, J. Neurosci 30 (2010) 14955–14963. [PubMed: 21068298]
5. Buchsbaum G, Gottschalk A, Trichromacy, opponent colours coding and optimum colour information transmission in the retina, Proc R Soc L. B Biol Sci 220 (1983) 89–113.
6. Schnaitmann C, Haikala V, Abraham E, Oberhauser V, Thestrup T, Griesbeck O, Reiff DF, Color Processing in the Early Visual System of *Drosophila*, Cell 172 (2018) 318–330.e18. [PubMed: 29328919]
7. Schnaitmann C, Garbers C, Wachtler T, Tanimoto H, Color Discrimination with Broadband Photoreceptors, Curr. Biol 23 (2013) 2375–2382. [PubMed: 24268411]
8. Gao S, ya Takemura S, Ting CY, Huang S, Lu Z, Luan H, Rister J, Thum AS, Yang M, Hong ST, Wang JW, Odenwald WF, White BH, Meinertzhagen IA, Lee CH, The Neural Substrate of Spectral Preference in *Drosophila*, Neuron 60 (2008) 328–342. [PubMed: 18957224]
9. Melnattur KV, Pursley R, Lin TY, Ting CY, Smith PD, Pohida T, Lee CH, Multiple redundant medulla projection neurons mediate color vision in *Drosophila*, J. Neurogenet 28 (2014) 374–388. [PubMed: 24766346]
10. Karuppudurai T, Lin TY, Ting CY, Pursley R, Melnattur KV, Diao F, White BH, Macpherson LJ, Gallio M, Pohida T, Lee CH, A Hard-Wired Glutamatergic Circuit Pools and Relays UV Signals to Mediate Spectral Preference in *Drosophila*, Neuron 81 (2014) 603–615. [PubMed: 24507194]
11. Yamaguchi S, Desplan C, Heisenberg M, Contribution of photoreceptor subtypes to spectral wavelength preference in Drosophila, Proc. Natl. Acad. Sci 107 (2010) 5634–5639. [PubMed: 20212139]
12. Hardie RC, Functional organization of the fly retina, in: Autrum H, Ottoson D, Perl ER, Schmidt RF, Shimazu H, Willis WD (Eds.), Progress in Sensory Physiology, Springer Berlin Heidelberg, Berlin, Heidelberg, 1985, pp. 1–79.
13. Behnia R, Desplan C, Visual circuits in flies: beginning to see the whole picture, Current Opinion in Neurobiology 34 (2015) 125–132. [PubMed: 25881091]
14. Clandinin TR, Zipursky S, Afferent Growth Cone Interactions Control Synaptic Specificity in the *Drosophila* Visual System, Neuron 28 (2000) 427–436. [PubMed: 11144353]
15. Thoreson WB, Mangel SC, Lateral interactions in the outer retina, Prog. Retin. Eye Res 31 (2012)407–441. [PubMed: 22580106]
16. Wernet MF, Velez MM, Clark DA, Baumann-klausener F, Brown JR, Klovstad M, Labhart T, Clandinin TR, Genetic Dissection Reveals Two Separate Retinal Substrates for Polarization Vision in *Drosophila*, Current Biology 22 (2012) 12–20. [PubMed: 22177904]
17. Kelber A, Vorobyev M, Osorio D, Animal colour vision - Behavioural tests and physiological concepts, Biol. Rev. Camb. Philos. Soc 78 (2003) 81–118. [PubMed: 12620062]
18. Renoult JP, Kelber A, Schaefer HM, Colour spaces in ecology and evolutionary biology, Biol. Rev 92 (2017) 292–315. [PubMed: 26468059]
19. Henderson SR, Reuss H, Hardie RC, Single photon responses in *Drosophila* photoreceptors and their regulation by Ca2+, J. Physiol 524 (2000) 179–194. [PubMed: 10747191]
20. Juusola M, Hardie RC, Light Adaptation in *Drosophila* Photoreceptors I: Response Dynamics and Signaling Efficiency at 25C, The Journal of General Physiology 117 (2001) 3–25. [PubMed: 11134228]
21. Takemura S.-y., Bharioke A, Lu Z, Nern A, Vitaladevuni S, Rivlin PK, Katz WT, Olbris DJ, Plaza SM, Winston P, Zhao T, Horne JA, Fetter RD, Takemura S, Blazek K, Chang L-A, Ogundeyi O, Saunders MA, Shapiro V, Sigmund C, Rubin GM, Scheffer LK, Meinertzhagen IA, Chklovskii

DB, A visual motion detection circuit suggested by Drosophila connectomics, Nature 500 (2013) 175–181. [PubMed: 23925240]

22. Davis FP, Nern A, Picard S, Reiser MB, Rubin GM, Eddy SR, Henry GL, A genetic, genomic, and computational resource for exploring neural circuit function, bioRxiv (2018).
23. Reiser M, Nern A, Zhao A, Longden K, Rubin G, Flynn M, Laughland C, Ludwig H, Parekh R, Colorvision2, 2019 URL: https://janelia.figshare.com/articles/colorVision2_pdf/9638825.
24. Nern A, Pfeiffer BD, Rubin GM, Optimized tools for multicolor stochastic labeling reveal diverse stereotyped cell arrangements in the fly visual system, Proc. Natl. Acad. Sci. U.S.A 112 (2015) E2967–E2976. [PubMed: 25964354]
25. Klapoetke NC, Murata Y, Kim SS, Pulver SR, Birdsey-Benson A, Cho YK, Morimoto TK, Chuong AS, Carpenter EJ, Tian Z, Wang J, Xie Y, Yan Z, Zhang Y, Chow BY, Surek B, Melkonian M, Jayaraman V, Constantine-Paton M, Wong GK-S, Boyden ES, Independent optical excitation of distinct neural populations, Nature Methods 11 (2014) 338–346. [PubMed: 24509633]
26. Fisher YE, Leong JC, Sporar K, Ketkar MD, Gohl DM, Clandinin TR, Silies M, A Class of Visual Neurons with Wide-Field Properties Is Required for Local Motion Detection, Current Biology 25 (2015) 3178–3189. [PubMed: 26670999]
27. Takemura S.-y., Xu CS, Lu Z, Rivlin PK, Parag T, Olbris DJ, Plaza S, Zhao T, Katz WT, Umayam L, Weaver C, Hess HF, Horne JA, Nunez-Iglesias J, Aniceto R, Chang L-A, Lauchie S, Nasca A, Ogundeyi O, Sigmund C, Takemura S, Tran J, Langille C, Le Lacheur K, McLin S, Shinomiya A, Chklovskii DB, Meinertzhagen IA, Scheffer LK, Synaptic circuits and their variations within different columns in the visual system of Drosophila, Proc. Natl. Acad. Sci 112 (2015) 13711–13716. [PubMed: 26483464]
28. Barlow HB, Possible Principles Underlying the Transformations of Sensory Messages, in: Rosenblith W (Ed.), Sens. Commun, MIT Press, Cambridge, 1961, pp. 216–234.
29. Atick JJ, Redlich AN, What Does the Retina Know about Natural Scenes?, Neural Computation 4 (1992) 196–210.
30. Vorobyev M, Brandt R, Peitsch D, Laughlin SB, Menzel R, Colour thresholds and receptor noise: behaviour and physiology compared, Vision Research 41 (2001) 639–653. [PubMed: 11226508]
31. Scheffer LK, Meinertzhagen IA, The Fly Brain Atlas, Annu. Rev. Cell Dev. Biol 35 (2019).
32. Stavenga DG, Angular and spectral sensitivity of fly photoreceptors. I. Integrated facet lens and rhabdomere optics., J. Comp. Physiol 189 (2003) 1–17. [PubMed: 12548425]
33. Hardie RC, Franceschini N, McIntyre PD, Electrophysiological analysis of fly retina, Journal of comparative physiology 133 (1979) 23–39.
34. Lennie P, Haake PW, Williams DR, The Design of Chromatically Opponent Receptive Fields, in: Landy M, Movshon JA (Eds.), Comput. Model. Vis. Process, MIT Press, Cambridge, 1991, pp. 71–81.
35. Crook JD, Manookin MB, Packer OS, Dacey DM, Horizontal Cell Feedback without Cone Type-Selective Inhibition Mediates “Red-Green” Color Opponency in Midget Ganglion Cells of the Primate Retina, J. Neurosci. 31 (2011) 1762–1772. [PubMed: 21289186]
36. Lee BB, Shapley RM, Hawken MJ, Sun H, Spatial distributions of cone inputs to cells of the parvocellular pathway investigated with cone-isolating gratings, J. Opt. Soc. Am. A 29 (2012) A223–A232.
37. Derrico JB, Buchsbaum G, A Computational Model of Spatiochromatic Image Coding in Early Vision, J. Vis. Commun. Image Represent 2 (1991) 31–38.
38. Atick JJ, Li Z, Redlich AN, Understanding Retinal Color Coding from First Principles, Neural Computation 4 (1992) 559–572.
39. Livingstone MS, Hubel DH, Anatomy and physiology of a color system in the primate visual cortex, J Neurosci 4 (1984) 309–356. [PubMed: 6198495]
40. Gegenfurtner KR, Kiper DC, Color Vision, Annu. Rev. Neurosci 26 (2003) 181–206. [PubMed: 12574494]
41. Takeuchi Y, Arikawa K, Kinoshita M, Color discrimination at the spatial resolution limit in a swallowtail butterfly, papilio xuthus, Journal of Experimental Biology 209 (2006) 2873–2879. [PubMed: 16857870]

42. Giurfa M, Vorobyev M, Kevan P, Menzel R, Detection of coloured stimuli by honeybees: minimum visual angles and receptor specific contrasts, Journal of Comparative Physiology A 178 (1996) 699–709.
43. Giurfa M, Vorobyev M, The angular range of achromatic target detection by honey bees, Journal of Comparative Physiology A 183 (1998) 101–110.
44. Salcedo E, Huber A, Henrich S, Chadwell LV, Chou W.-h., Paulsen R, Britt SG, Blue- and Green-Absorbing Visual Pigments of *Drosophila*: Ectopic Expression and Physiological Characterization of the R8 Photoreceptor Cell-Specific Rh5 and Rh6 Rhodopsins, J. Neurosci 19 (1999)10716–10726. [PubMed: 10594055]
45. Govardovskii VI, Fyhrquist N, Reuter T, Kuzmin DG, Donner K, In search of the visual pigment template, Visual Neuroscience 17 (2000) 509–528. [PubMed: 11016572]
46. Cook T, Pichaud F, Sonneville R, Papatsenko D, Desplan C, Distinction between Color Photoreceptor Cell Fates Is Controlled by Prospero in *Drosophila*, Developmental Cell 4 (2003) 853–864. [PubMed: 12791270]
47. Saint-Charles A, Michard-Vanhee C, Alejevski F, Chelot E, Boivin A, Rouyer F, Four of the six *Drosophila* rhodopsin-expressing photoreceptors can mediate circadian entrainment in low light, J. Comp. Neurol 524 (2016) 2828–2844. [PubMed: 26972685]
48. Vasiliauskas D, Mazzoni E, G Sprecher S, Brodetskiy K, Johnston R, Lidder P, Vogt N, Celik A, Desplan C, Feedback from Rhodopsin controls rhodopsin exclusion in *Drosophila* photoreceptors, Nature 479 (2011) 108–12. [PubMed: 21983964]
49. Alejevski F, Saint-Charles A, Michard-Vanhee C, Martin B, Galant S, Vasiliauskas D, Rouyer F, The HisCl1 histamine receptor acts in photoreceptors to synchronize Drosophila behavioral rhythms with light-dark cycles, Nature Communications 10 (2019) 252.
50. Tahayato A, Sonneville R, Pichaud F, Wernet MF, Papatsenko D, Beaufils P, Cook T, Desplan C, Otd/crx, a dual regulator for the specification of ommatidia subtypes in the drosophila retina, Developmental Cell 5 (2003) 391–402. [PubMed: 12967559]
51. Behnia R, Clark DA, Carter AG, Clandinin TR, Desplan C, Processing properties of ON and OFF pathways for *Drosophila* motion detection., Nature 512 (2014) 427–430. [PubMed: 25043016]
52. Mazzoni EO, Celik A, Wernet MF, Vasiliauskas D, Johnston RJ, Cook TA, Pichaud F, Desplan C, Iroquois complex genes induce co-expression of rhodopsins in Drosophila, PLoS Biol. 6 (2008) e97. [PubMed: 18433293]
53. Morante J, Desplan C, Dissection and staining of Drosophila optic lobes at different stages of development, Cold Spring Harb. Protoc 2011 (2011) 652–656. [PubMed: 21632779]
54. von Kries J, Die Gesichtsempfindungen, in: Nagel W (Ed.), Handbuch der Physiologie des Menschen, volume 3, Vieweg und Sohn, Braunschweig, 1904, pp. 109–282.
55. Kelber A, Osorio D, From spectral information to animal colour vision: Experiments and concepts, Proc. R. Soc. B Biol. Sci 277 (2010) 1617–1625.
56. Giovannucci A, Friedrich J, Gunn P, Kalfon J, Brown BL, Koay SA, Taxidis J, Najafi F, Gauthier JL, Zhou P, Khakh BS, Tank DW, Chklovskii DB, Pnevmatikakis EA, CalmAn: An open source tool for scalable Calcium Imaging data Analysis, eLife 8 (2019) e38173. [PubMed: 30652683]
57. Menzel R, Shmida A, The ecology of flower colours and the natural colour vision of insect pollinators: The israeli flora as a study case, Biological Reviews 68 (1993) 81–120.
58. Chittka L, Shmida A, Troje N, Menzel R, Ultraviolet as a component of flower reflections, and the colour perception of hymenoptera, Vision Research 34 (1994) 1489–1508. [PubMed: 8023461]
59. Chittka L, Optimal sets of color receptors and color opponent systems for coding of natural objects in insect vision, Journal of Theoretical Biology 181 (1996) 179–196.
60. Chittka L, Bee color vision is optimal for coding flower color, but flower colors are not optimal for being coded: Why?, Israel Journal of Plant Sciences 45 (1997) 115–127.
61. Gumbert A, Kunze J, Chittka L, Floral colour diversity in plant communities, bee colour space and a null model, Proceedings: Biological Sciences 266 (1999) 1711–1716.
62. Garbers C, Wachtler T, Wavelength discrimination in Drosophila suggests a role of rhodopsin 1 in color vision, PLOS ONE 11 (2016) 1–20.
63. Yatsenko D, Walker EY, Tolias AS, Datajoint: A simpler relational data model, arXiv (2018).

64. Hong S-T, Bang S, Paik D, Kang J, Hwang S, Jeon K, Chun B, Hyun S, Lee Y, Kim J, Histamine and its receptors modulate temperature-preference behaviors in drosophila, Journal of Neuroscience 26 (2006) 7245–7256. [PubMed: 16822982]

65. Barrett A, Krueger S, Jackson M, Datta S, Curable genetic instability of a gal4 transgene in drosophila, Fly 2 (2008) 67–73. [PubMed: 18820434]

Highlights

- Surround inhibition contributes to color opponency in fly photoreceptor axons
- This inhibition is mediated by the horizontal-cell-like medulla interneuron Dm9
- The resulting circuit produces an efficient representation of chromatic information
- A biologically constrained model predicts a complex spatio-chromatic receptive field

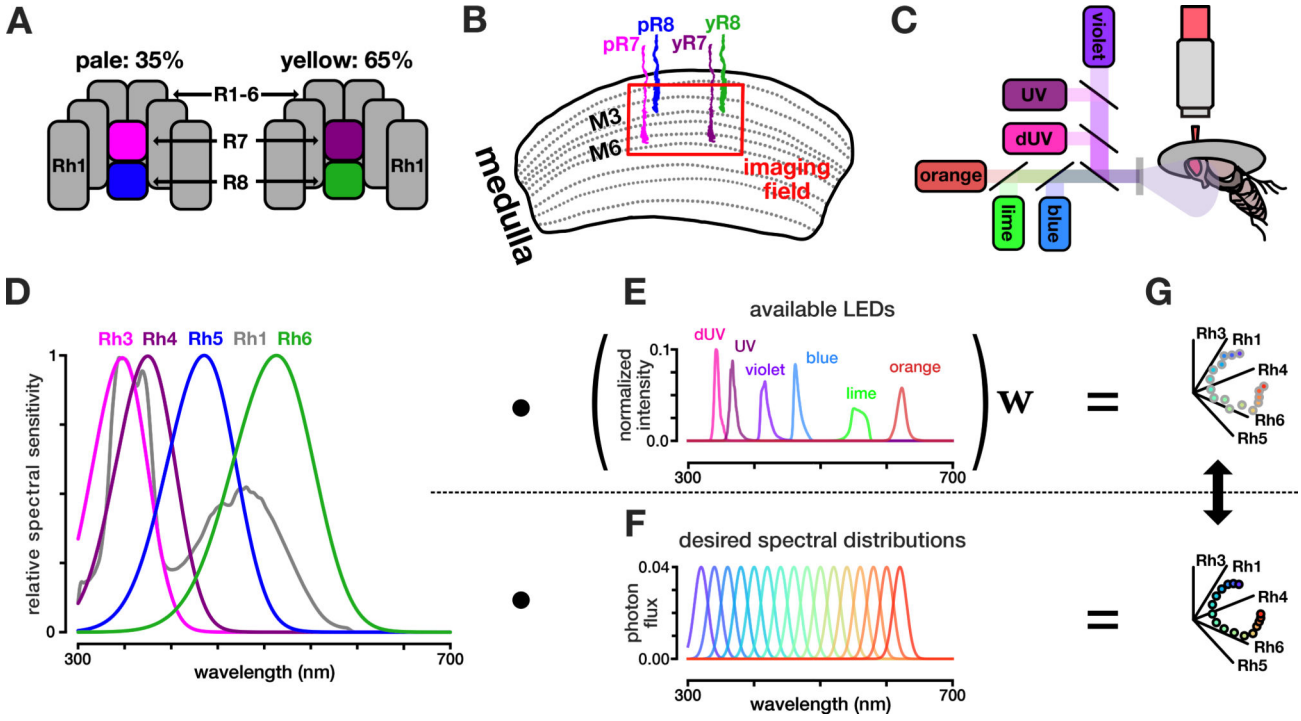

Figure 1. Experimental setup and stimulus design.

A. Spectral composition of pale and yellow ommatidia of the *Drosophila* eye. Pale ommatidia express Rh3 and Rh5 in R7 and R8, respectively. Yellow ommatidia express Rh4 and Rh6 in R7 and R8, respectively. R1–6 all express Rh1. **B.** Photoreceptors in *Drosophila* project from the retina into the optic lobe. Our imaging experiments target the axon terminals of R7 and R8 in the medulla at the level of layers M6 and M3, respectively. **C.** Two-photon imaging set up. The fly is secured facing LED setup, and LED sources are combined using a custom color mixer to form a single collimated beam. **D.** Relative spectral sensitivity of opsins expressed in the fruit fly retina; data from [44] and fitted with equation from [45] (see STAR methods). **E.** Normalized photon flux across the wavelength spectrum, corresponding to the various LEDs used for stimuli. **F.** Desired set of spectral distributions to test to build a spectral tuning curve. **G.** For any given single wavelength in **F,** we calculate the relative photon capture (q) for all five opsins by integrating over the opsin sensitivities in **D,** and plot a vector in photon capture space. We then simulate the single wavelength with combinations of the available LEDs in **E** that most closely recreate that vector (see STAR methods for details). See also Figure S1 and Table S1.

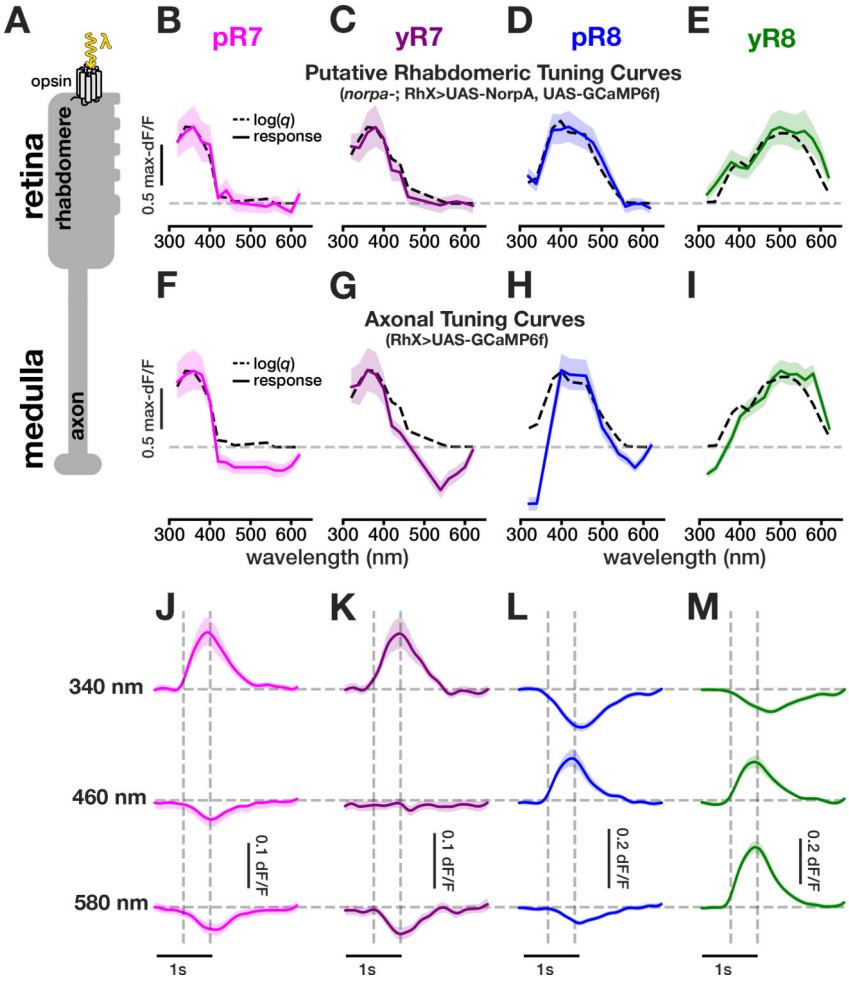

Figure 2. R7 and R8 putative rhabdomeric responses are transformed into opponent outputs.

A. In *Drosophila* photoreceptors, light (λ) is absorbed in the retina by rhodopsin molecules at the level of the rhabdomeres, where phototransduction takes place. Photoreceptors project their axons to the medulla where synaptic interactions occur. **B-E.** NorpA, an essential component of the phototransduction cascade, was restored in *norpa-* blind flies in individual photoreceptor types (RhX denoting Rh3/4/5/6). This allowed for measurement of putative rhabdomeric spectral tuning in photoreceptor axons by eliminating interactions from other cell types. Max-normalized responses of R7/R8 axons were measured across simulated wavelengths to construct spectral tuning curves. ROIs correspond to individual cells, whose responses were averaged equally across flies. Ns= 106 ROIs (8 flies), 96(8), 69(7), and 26(4), respectively. Dashed black lines represent the log (*q*). Colored lines represent the mean photoreceptor response. Shaded region represents the 95% confidence interval. Dashed grey lines represent baseline fluorescence. **F-I.** Max-normalized spectral tuning curves constructed using the amplitudes of measured responses of R7 and R8 axons in wild type flies. Ns= 152(8), 134(6), 138(7), and 129(6), respectively. **J-M.** Average GCaMP6f responses of R7 and R8 axons in wild type flies to 0.5 second flashes of three simulated wavelengths. Vertical dashed grey lines represent onset and offset of light presentation. See also Table S1.

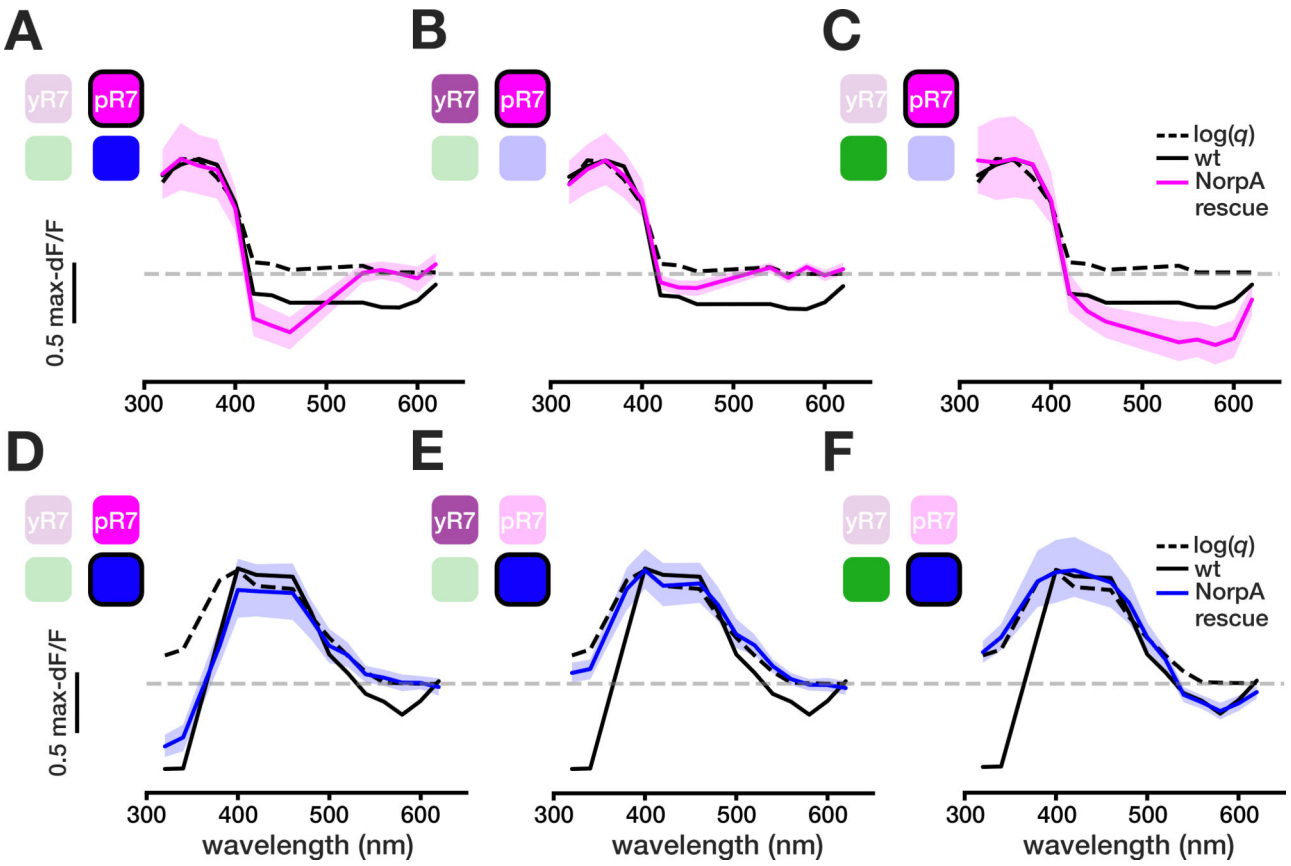

Figure 3. Pairwise NorpA rescues highlight sources of opponency in R7/R8.

NorpA, a component of the phototransduction cascade, was restored in *norpa*- blind flies in select pairs of photoreceptor types to determine contributions to opponency. **A-C.** Max-normalized responses of pR7 axons were measured across simulated wavelengths, with NorpA restored in pR7 and a second indicated photoreceptor type. Ns= 106 ROIs (8 flies), 108(8), 132(8), and 104(6), respectively. Dashed black lines represent log (*q*), black lines represent the wild type response, colored lines represent the mean photoreceptor response, shaded regions represents the 95% confidence interval, dashed grey lines represent baseline fluorescence. **D-F.** Max-normalized responses of pR8 axons were measured across simulated wavelengths, with NorpA restored in pR8 and a second indicated photoreceptor type. Ns= 63(7), 80(9), 69(7), and 63(7), respectively. See also Figure S2 and Table S1.

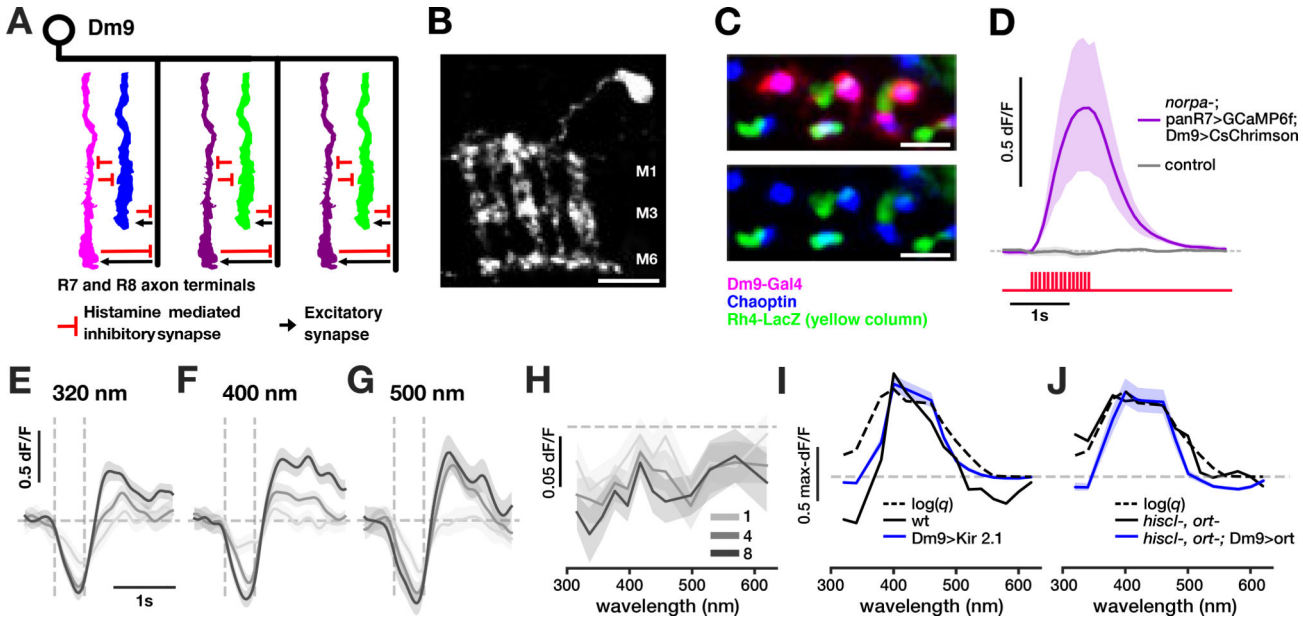

Figure 4. The horizontal cell-like interneuron Dm9 mediates indirect spectral opponency.

A. Schematic of Dm9/photoreceptor connectivity. Dm9 is an excitatory interneuron spanning multiple medulla columns shown to be both pre- and postsynaptic to R7/R8. **B.** Side view of a maximum projection of a single Dm9 clone (R32E04-Gal4). Scale bar: 10 μm **C.** Cross section view of a single Dm9 clone (pink), photoreceptor terminals (blue), and yR7 terminals (green) shows a single Dm9 contacts both yellow and pale ommatidia. Scale bar: 5 μm **D.** Purple trace represents GCaMP6f Responses in R7 after a pulse train of red light in flies expressing CsChrimson in Dm9 (R32E04 driver) N= 37 (4 flies). Grey trace represents R7 responses in control flies without CsChrimson expression. N= 70 (5 flies). Solid lines represent the mean, shaded region represents 95% confidence interval. Vertical red lines represent light presentation. Horizontal dashed grey lines represent baseline fluorescence. **E-G.** Responses of Dm9 (R32E04-Gal4) to 0.5 second flashes of three simulated wavelengths over a 10 μE background with a flat spectrum. Responses to three luminant multiples of each wavelength are shown (1x, 4x, and 8x). Solid lines represent the mean, shaded region represents 95% confidence interval. Vertical dashed grey lines represent onset and offset of light presentation. Horizontal dashed grey lines represent baseline fluorescence. **H.** Dm9 spectral tuning curves corresponding to three luminant multiples of each wavelength are shown (1x, 4x, and 8x). **I.** pR8 max-normalized spectral tuning curves. Blue line represents pR8 responses in a Dm9-silenced background (R32E04-Gal4 driving UAS-Kir2.1) N= 323 ROIs (6 flies). Black line represents wild type pR8 responses using the same GCaMP6f construct. Dashed black lines represent the log (q). **J.** pR8 max-normalized spectral tuning curves. Blue line represents pR8 tuning in a *hiscl-,ort-* mutant background where Ort was rescued in Dm9 (R21A12-GaL4 driving UAS-Ort) N= 153 (6). Black line represents pR8 in a *hiscl-,ort-* mutant background. Dashed black lines represent the log (q). See also Figure S3 and Table S1.

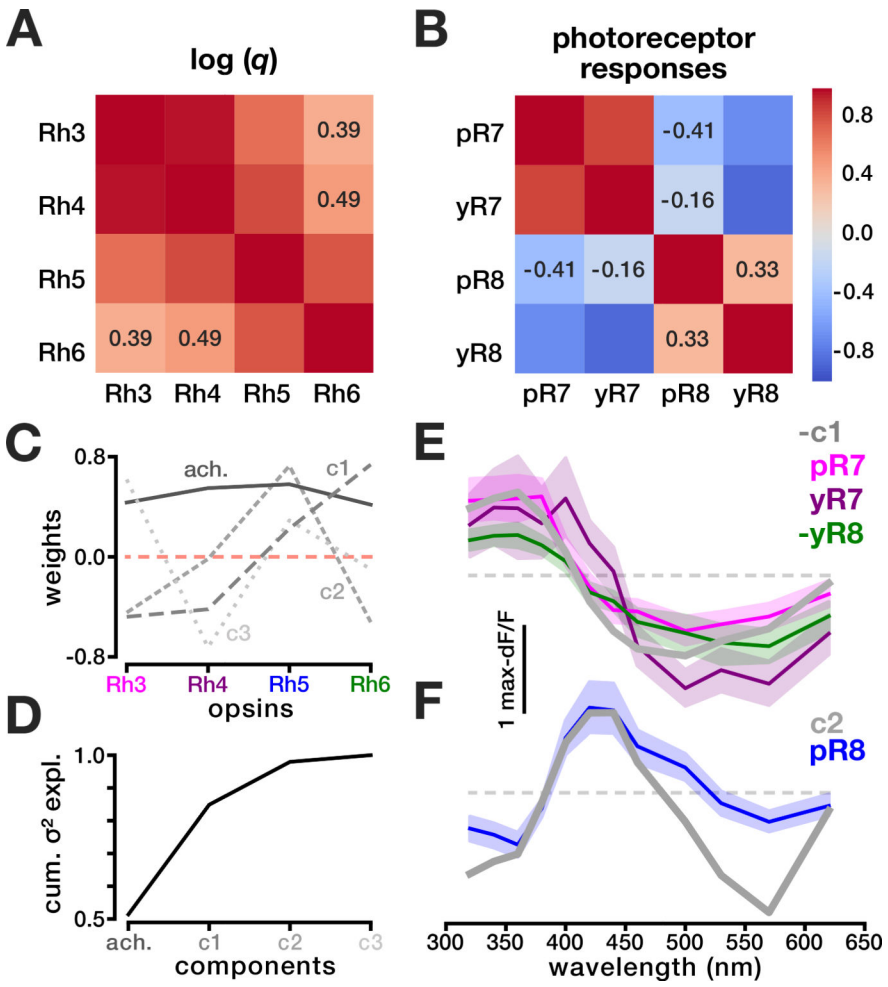

Figure 5. Opponency is consistent with principal components which efficiently decorrelate and preserve chromatic information.

A. Correlation matrix comparing the calculated rhabdomeric responses of R7s and R8s. **B.** Correlation matrix comparing the measured axonal responses in R7 and R8 outputs. **C.** Decomposition of opsin spectral sensitivities using principal component analysis (PCA) yields four main principal components : an achromatic component (ach) and three chromatic components (c1, c2, and c3) **D.** Percentage of the variance explained by each principal component. **E-F.** Comparisons between the max-normalized tuning curves based on the measured tuning curves in R7 and R8 axons (colored lines) and the first two chromatic components c1 and c2 (gray lines) to the flat background for luminant multiple 4 (see Figure S4). See also Figure S5 and Table S1.

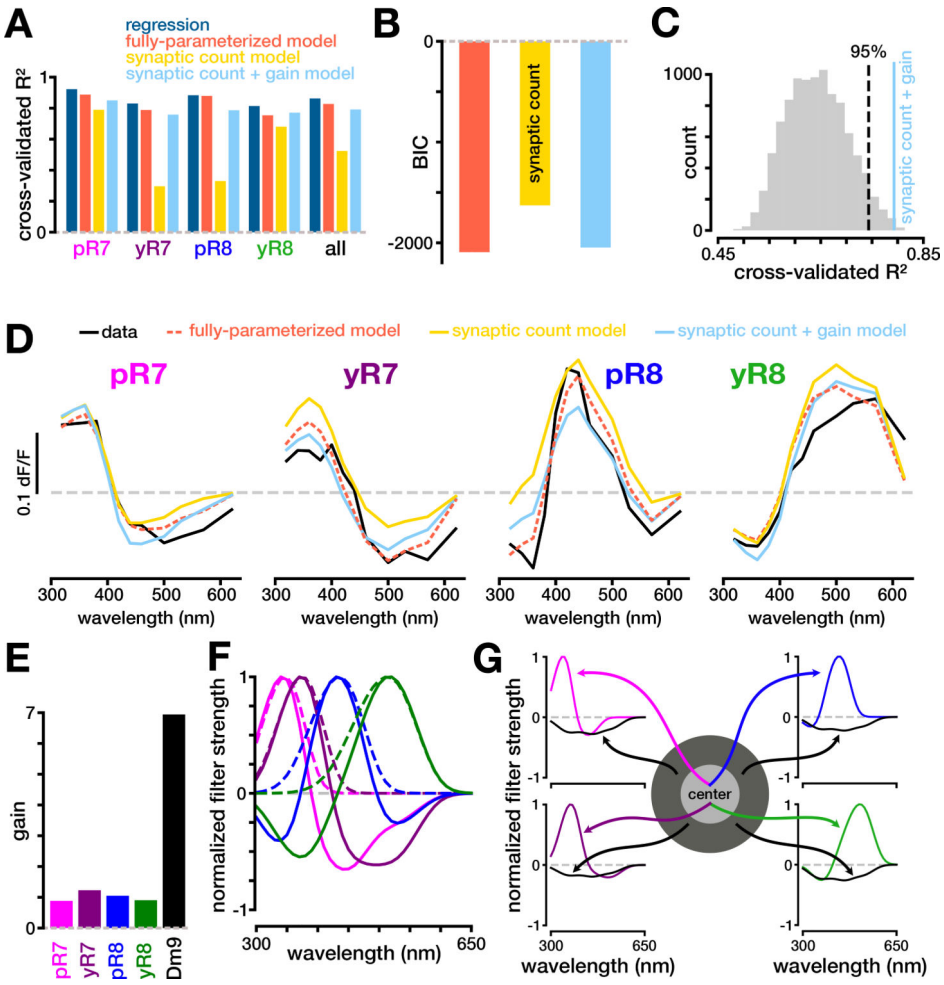

Figure 6. Recurrent model of color opponency in R7 and R8 photoreceptors.

A. Comparison of different cross-validated R^2 values using linear regression, the fully-parameterized recurrent model, the synaptic count recurrent model, and the synaptic count + gain recurrent model. **B.** Comparison of BIC values for the different iterations of the recurrent model. **C.** Distribution of R^2 values using random weights for the synaptic count + gain model. The dotted line indicates the 95th percentile of the distribution and the solid colored line indicates the R^2 value using the synaptic counts as weights. **D.** Predicted responses for the different iterations of the recurrent model (colored), and the actual mean response of the photoreceptor in question (black). **E.** Fitted gains for different neurons in the recurrent circuit for the synaptic count + gain model. **F.** The predicted spectral filtering properties of the different photoreceptor outputs (solid line) compared to the filtering properties of the rhodopsin they express (dashed line). **G.** The spectral filtering properties for the predicted center and surround of the different photoreceptor outputs. See also Figure S4, Figure S6, Table S1, and Table S2.